6-1-2012

A small scale energy harvester from wind induced vibrations

Ahmed Sayed Ahmed Abdel-Fattah

The American University in Cairo

The School of Sciences and Engineering

A SMALL-SCALE ENERGY HARVESTER FROM WIND INDUCED VIBRATIONS

A Thesis Submitted to

Mechanical Engineering Department

in partial fulfillment of the requirements for

the degree of Master of Science

Mechanical Design

by Ahmed Sayed Abdel-Fattah

under the supervision of Dr. Mustafa Arafa

May/2012

ABSTRACT

In this study, a new device for wind energy harvesting on a small-scale was proposed. This system is well suited for powering remote wireless sensors as a cheaper, more environmentally friendly alternative to conventional dry cell batteries which is a need that is being addressed by many recent research studies. The device consists of a cantilever beam with the free end attached to a square section box that is subjected to the air stream inducing aero-elastic flutter. Flutter is a coupled torsion, plunge instability that has been historically studied to be avoided by aerospace and civil engineers. A magnet is attached to the beam and a stationary coil is used to generate electrical power. A finite element model for the device was achieved by formulating a set of ordinary differential equations that integrate the mechanical model of the beam with the aero-elastic flutter of the square section at the tip and the electromagnetic effect of the energy harvesting coil, and they were numerically solved. Wind tunnel experiment runs were carried out for a system with a 30 cm beam and a 30 cm long 5cm wide cross section for wind speeds of 2.4 to 3.2 m/s and electric loads of 40 Ω to 4 MΩ. The numerical predictions were found to compare favorably with the experimental results in terms of the induced voltage, frequency, and power output.

TABLE OF CONTENTS

LIST OF FIGURES iv
LIST OF TABLES vi
NOMENCLATURE vii
1 INTRODUCTION AND LITRETURE REVIEW 1
1.1 Energy Harvesting Techniques 1
1.2 Using Mechanical Vibrations to Induce Current 2
1.3 Wind Energy 3
1.4 Motivation 3
1.5 Literature Review 4
1.6 Aerodynamic Instability Phenomena 13
1.7 Research Objectives 16
1.8 Thesis Organization 17
2 HARVESTER DESIGN AND MODELING 18
2.1 Harvester Design 18
2.2 Purpose of the Finite Element Model 19
2.3 Model for the System Structure 19
2.4 Aero-elastic Model 21
2.5 Electromagnetic Model 23
2.6 Governing Equations 25
3 EXPERIMENTAL WORK 28
3.1 Experimental Setup 28
3.2 Experimental Procedure 30
4 RESULTS 31
4.1 Transient Response comparisons 31
4.2 Frequency Comparisons 31
4.3 Voltage and Power Comparisons at Steady State 33
4.4 Tip Displacement and Tip Rotation 33
5 CONCLUSIONS 39

APPENDIX A: DERIVATION OF BEAM MASS AND STIFFNESS MATRICES 44
APPENDIX B: TIME DOMAIN VOLTAGE PLOTS FOR THE REMAINING MODEL VERIFIED EXPERIMENTAL RUNS 47

LIST OF FIGURES

Figure 1: Magnus Effect Wind generator [8] 5
Figure 2: The lift force as it varies with the angular movement of the wing [10] 6
Figure 3: Front and top views of the flutter engine [10] 6
Figure 4: The electromagnetic harvester devised by Wang et al. [11] 7
Figure 5: VIVACE system [12] to the left is a proposed configuration for a plant and to the right is a detail showing a single cylinder 8
Figure 6: The Micro-Scale Windbelt developed by Shawn Frayne that can power light and temperature sensors [13] 8
Figure 7: The design of the flutter-mill devised by Tang et al., [14] 9
Figure 8: A Schematic of the flapping foil Energy Harvester [16] 10
Figure 9: The experimental setup used by Jung et al., [17] 11
Figure 10: Operation Concept of the Micro-Power Generator devised by Bibo et al., [18] 11
Figure 11: Galloping Energy harvester devised by Sirohi and Mahadik [19] 12
Figure 12: The flutter of Tacoma Narrows Bridge before its collapse [20] 13
Figure 13: A comparison between amplitude variation with velocity curves of different aerodynamic instability phenomena adopted from Jung and Lee [21] 14
Figure 14: The slender cross sections for which resulting wind force directions cause galloping [23] 15
Figure 15: Schematic illustration of proposed design (top view) 19
Figure 16: The Deformed configuration of the beam element adopted from [25] 20
Figure 17: Air loads acting on square section 21
Figure 18: Variation in lift and drag coefficients with time [27] 23
Figure 19: A flowchart for the solution process of the numerical model 27
Figure 20 Experimental Setup 28
Figure 21: On top is the model predicted time response for the system using 100 ohm resistance at the wind speed of 3.2 m/s and below it is the experimentally measured response for it 32
Figure 22: Graphs showing the correlation between the experimental (denoted by *) and the model predictted values (denoted bu (-) for the volt (in the top drawing) and the power (in the bottom drawing) for different values of load resistance for wind speed of 2.3 m/s 34

Figure 23: Graphs showing the correlation between the experimental (denoted by *) and the model predictted values (denoted bu (-) for the volt (in the top drawing) and the power (in the bottom drawing) for different values of load resistance for wind speed of 2.7 m/s 35
Figure 24: Graphs showing the correlation between the experimental (denoted by *) and the model predictted values (denoted bu (-) for the volt (in the top drawing) and the power (in the bottom drawing) for different values of load resistance for wind speed of 3.2 m/s 36
Figure 25: Model predicted tip displacement time plots where the electromagnetic effect and the magnet mass are removed and they are present in the bottom drawing 37
Figure 26: Model predicted tip displacement time plots where the electromagnetic effect and the magnet mass are removed and they are present in the bottom drawing 38
Figure 27: On top is the model predicted time response for the system using 40 ohm resistance at the wind speed of 2.3 m/s and below it is the experimentally measured response for it 47
Figure 28: On top is the model predicted time response for the system using 100 ohm resistance at the wind speed of 2.3 m/s and below it is the experimentally measured response for it 48
Figure 29: On top is the model predicted time response for the system using 400 ohm resistance at the wind speed of 2.3 m/s and below it is the experimentally measured response for it 49
Figure 30: On top is the model predicted time response for the system using 4 Kohm resistance at the wind speed of 2.3 m/s and below it is the experimentally measured response for it 50
Figure 31: On top is the model predicted time response for the system using 4 Mohm resistance at the wind speed of 2.3 m/s and below it is the experimentally measured response for it 51
Figure 32: On top is the model predicted time response for the system using 40 ohm resistance at the wind speed of 2.7 m/s and below it is the experimentally measured response for it 52
Figure 33: On top is the model predicted time response for the system using 100 ohm resistance at the wind speed of 2.7 m/s and below it is the experimentally measured response for it 53
Figure 34: On top is the model predicted time response for the system using 400 ohm resistance at the wind speed of 2.7 m/s and below it is the experimentally measured response for it 54
Figure 35: On top is the model predicted time response for the system using 4 Kohm resistance at the wind speed of 2.7 m/s and below it is the experimentally measured response for it 55

Figure 36: On top is the model predicted time response for the system using 4 Mohm resistance at the wind speed of 2.7 m/s and below it is the experimentally measured response for it 56
Figure 37: On top is the model predicted time response for the system using 40 ohm resistance at the wind speed of 3.2 m/s and below it is the experimentally measured response for it 57
Figure 38: On top is the model predicted time response for the system using 400 ohm resistance at the wind speed of 3.2 m/s and below it is the experimentally measured response for it 58
Figure 39: On top is the model predicted time response for the system using 4 Kohm resistance at the wind speed of 3.2 m/s and below it is the experimentally measured response for it 59
Figure 40: On top is the model predicted time response for the system using 4 Mohm resistance at the wind speed of 3.2 m/s and below it is the experimentally measured response for it 60

LIST OF TABLES

Table 1: Properties used for the experimental results..... 29

NOMENCLATURE

A	Beam cross section area
b	Geometrical characteristic (Section width × Length)
B	Electro-magnetic flux
$[C]$	Damping matrix
C_D	Drag coefficient
C_L	Lift coefficient
D	Drag force
D_{Cu}	Coil wire diameter
D_i	Coil inner diameter
D_o	Coil outer diameter
E	Modulus of elasticity
$\{F\}$	Force Vector
F_A	Aero-elastic force
F_n	Electro-magnetic force
h_b	Coil height
i	Electric current
I	Second moment of area for the beam section
$[K]$	Stiffness matrix
l	Length in the beam direction
L	Lift force
L_c	Coil inductance
l_w	Coil wire length
$[M]$	Mass matrix
N	Number of coil turns
R_C	Coil resistance
R_L	Load resistance
U	Mean air velocity
U_{rel}	Relative air velocity
V	Voltage drop across the load resistance
$\{v\}$	vector of nodal speeds
v_n	Speed of the node where the magnet is present
w	Transverse displacement
α	angle between actual air velocity and relative air velocity
β	Stiffness matrix coefficient
γ	Mass matrix coefficient

$\{\delta\}$	Nodal degrees of freedom
θ	Torsional displacement (cross-section rotation)
μ_0	Air permeability
ρ	Beam density
ρ_{air}	Air density
ρ_{Cu}	Copper resistivity
subscript	
e	Element related

1 INTRODUCTION AND LITRETURE REVIEW

1.1 Energy Harvesting Techniques

Energy harvesting techniques rely on the generation of energy from existing ambient energy sources that are otherwise not utilized in that capacity. Energy harvesting has witnessed a significant growth in the past few years due to the increasing quest to use clean technologies to produce energy from renewable and abundant sources. One promising technology is to provide sustainable energy for portable low-power electronic devices in an attempt to reduce their reliance on batteries which normally have a limited lifespan and require periodic replacement. Developing small-scale renewable energy systems is a topic that has been investigated in many previous research works. The main concern for such research is how to make the power generating technology as efficient and economical as possible. The integration of energy harvesting devices with wireless sensor networks, such as traffic and weather sensors, can have a significant impact on the implementation of this technology, especially if self-powered devices can be developed at low cost and deployed in inaccessible or potentially hostile environments to transmit signals to receiving stations over an extended period of time. The technology can also have a tremendous impact if these devices could be utilized to provide electric power for remote residential communities deprived of electricity from the grid.

1.2 Using Mechanical Vibrations to Induce Current

A number of ambient energy sources have been recognized to be promising for energy harvesting, including heat waste, mechanical vibration, wind, solar energy, rainfall, human movement, seismic forces, traffic, and sea waves. While most of these sources can be exploited for energy harvesting, mechanical vibration seems particularly appealing due to the convenience of directly converting mechanical energy into electrical energy through various well-established transducers. In this context, vibration-based energy harvesters relying on electromagnetic [1], piezoelectric [2], electrostatic [3] and hybrid [4] principles have been reported. A vibration-based energy harvester typically consists of an elastic element that vibrates relative to a housing when subjected to external forces or base motion. In electromagnetic energy generation, for example, energy is generated by attaching a magnet to a vibrating spring-loaded mass in such a manner that it oscillates past an electric coil to generate electrical energy.

A review of the pertinent literature reveals that most of the reported studies are based on the fact that mechanical vibration is readily available as a source of energy at our disposal. Emphasis in many of studies was placed upon developing effective means to convert mechanical energy, typically provided by a dynamic shaker in a lab, into more useful forms of energy. These shaker tests provide useful tools to assess the performance of the developed devices at favorable drive conditions. However, mechanical vibration generally does not exist on its own by nature which is a limitation on the development of a truly sustainable energy harvester, unless a renewable energy source can be exploited to generate that mechanical vibration.

1.3 Wind Energy

Wind power can be harvested in several forms. For many years, the generation of renewable energy from wind has been centered on the use of rotating machinery, primarily wind turbines. While wind farms are known to be an effective means to generate power, their use in developing countries is faced with several challenges, including prohibitive costs of infrastructure, including land, civil work, electrical work, transmission lines and approach roads. In addition, the cost of the wind turbines often poses a financial burden for the governments and investors. The current market would therefore welcome innovative ideas aiming at the development of cost-effective, compact and efficient means of energy generation mechanisms that can possibly fit in remote areas without the need for expensive dedicated machinery that need to be strategically located in places that may be hard to access.

1.4 Motivation

Technological advances resulted in the use of many new small wireless energy efficient electronic sensing devices. These devices are generally powered by dry cell batteries that need frequent replacement and recharging. In order to power such devices extensive research is ongoing in order to achieve an economic system to harvest, otherwise wasted, energy from the ambient environment. Systems that use wind energy in order to induce mechanical vibrations have been the focus of many of these recent studies. Such a system can be suited to developing countries such as Egypt, as it shall be cheap to make on a small scale avoiding the use of small rotors and bearings that make

similar scale wind turbines impractical to use. It can also be a more environment friendly replacement for batteries in applications where wind is abundant.

Around 200 million dry cell batteries are spent in Egypt annually [5]. Improper disposal of these spent batteries to the landfill results in the contamination of the underground water with chemicals leaking out of them such as mercury and zinc oxides [6]. Being able to replace even a small percentage of the number of batteries used annually with a cheaper, and less polluting alternative will make substantial amount of saving in addition to the positive environmental impact to such an alternative. At a small scale conventional wind turbines become an expensive solution as they require small delicate bearings. Wind turbines also tend to have low efficiency at smaller scale [7].

1.5 Literature Review

In 1984, Dag Pike [8] showed how wind can be used to generate energy as rotors tend to move due to the pressure difference that is generated during their rotation according to what is known as the Magnus effect (Figure 1). However, for the system to work, it needs small DC motors to power each of the rotors. Then a greater amount of energy will be generated when the entire assembly of rotors starts to move. This system is also expensive and hard to shrink for smaller scale as it would still be hard to make smaller motors and bearings.

The idea of using fluid flow induced vibrations to generate power was introduced by Mckinney and DeLaurier [9] in 1981 when wind tunnel tests were performed on a symmetrical wing with an airfoil cross section that is free to translate vertically and use

the output to produce energy. The process efficiency was found to be comparable to the efficiencies of a regular windmill.

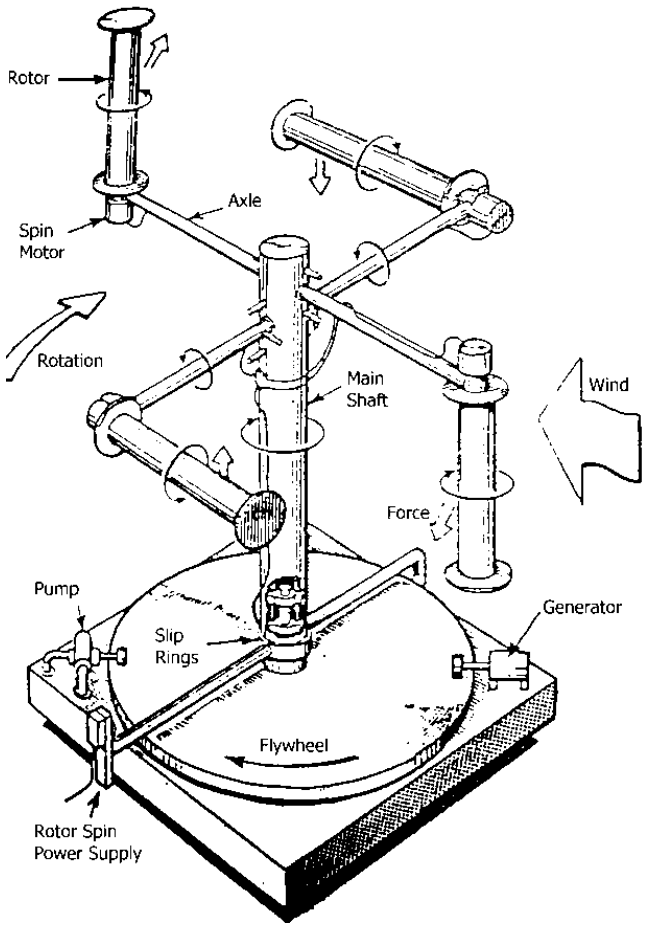

Figure 1: Magnus Effect Wind generator [8]

A similar design was used by Jones et al. [10] in 2003. However, the wing was immersed in a water tunnel. The model they developed took into account both the vertical translation of the wing and the angular displacement, providing a clearer explanation for the lift forces associated with the flutter angle as shown in Figure 2. The experimental design consisted of two wings that were allowed to move vertically and rotate; they were

installed to be out of phase and their motion was converted into rotary motion through the mechanism shown in Figure 3.

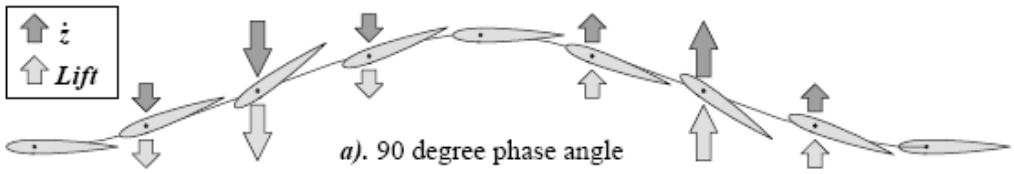

Figure 2: The lift force as it varies with the angular movement of the wing [10]

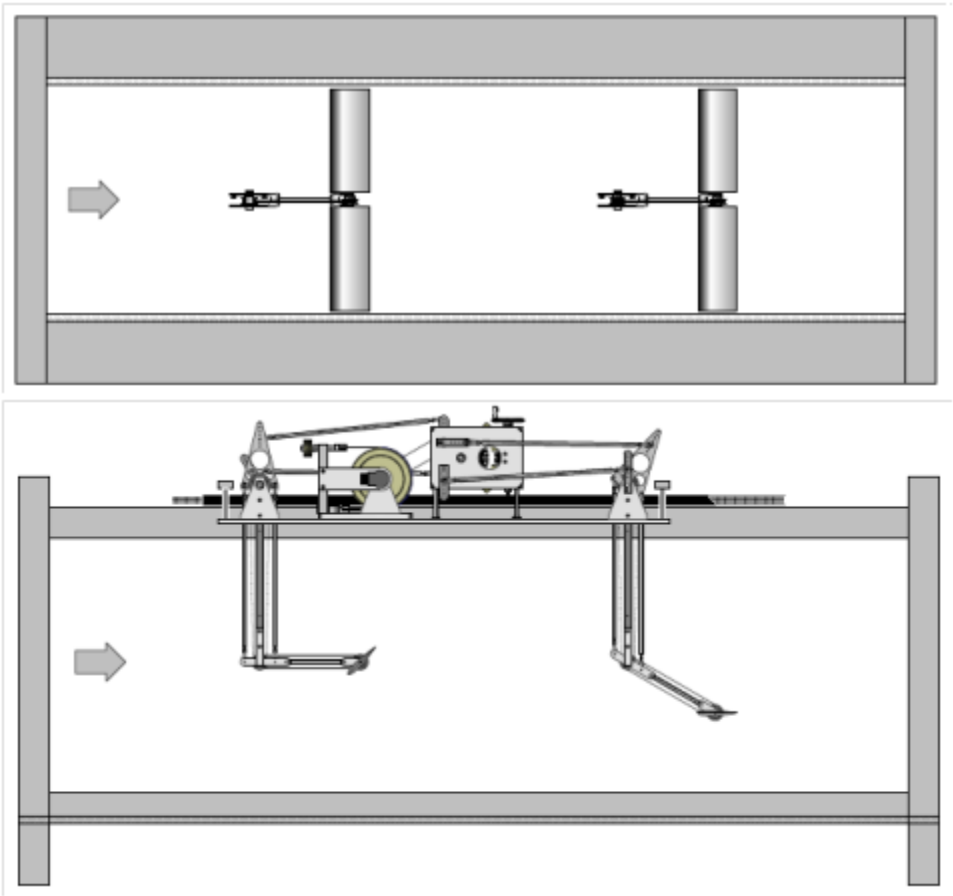

Figure 3: Front and top views of the flutter engine [10]

Wang et al. [11] proposed a system that uses the phenomenon of Kármán vortex in a water channel to generate power. A bluff body was placed in the water stream and

the vortices formed downstream of it were used to move a diaphragm (Figure 4). A magnet is fixed over the diaphragm and a stationary coil is placed near it in order to induce current. A prototype of a volume of 37.9 cm^3 of the system was tested and a power of 1.77 μW was obtained.

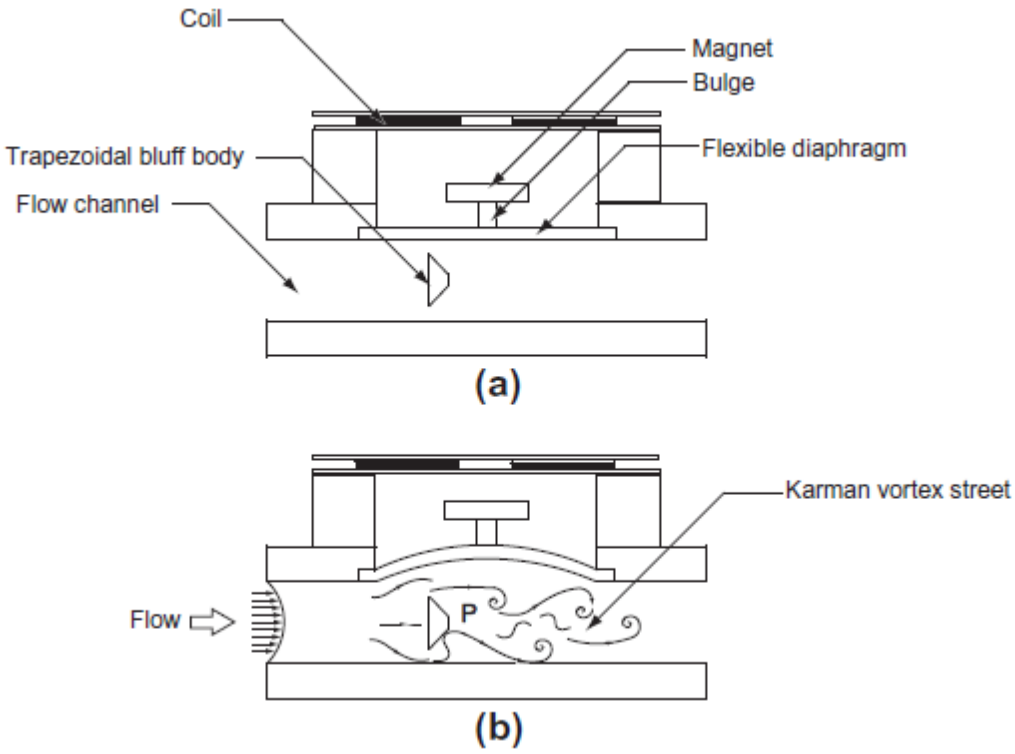

Figure 4: The electromagnetic harvester devised by Wang et al. [11]

Bernitsas et al. [12] introduced a new concept for harnessing the energy of ocean waves by using the phenomenon of vortex shedding; it was named Vortex Induced Vibration Aquatic Clean Energy VIVACE. This system consists of rigid cylinders mounted on elastic springs (Figure 5). A transmission mechanism is used to connect the cylinders to power take-off system. A model was devised for the system and verified using a free surface water channel prototype.

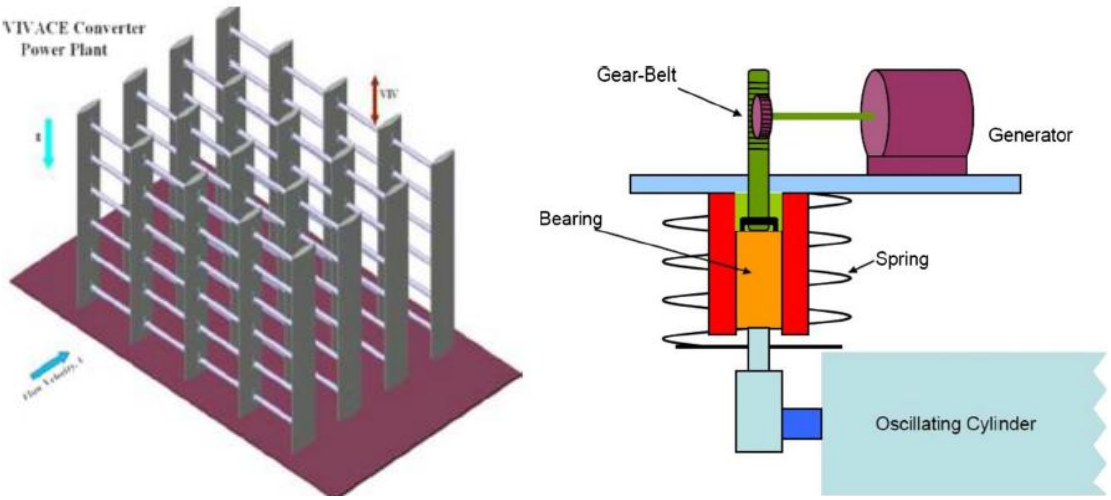

Figure 5: VIVACE system [12] to the left is a proposed configuration for a plant and to the right is a detail showing a single cylinder

In 2007, Shawn Frayne [7, 13], invented a mechanism that relied on the theory of aerodynamic flutter. This time the mechanism was a flexible belt under tension that would undergo angular and transverse vibrations due to the lift forces that arise from the pressure difference existing because of the fluid flow. A magnet was attached to one end of the taut belt and fixed a coil near that end in order to generate electricity on a small scale as shown in Figure 6.

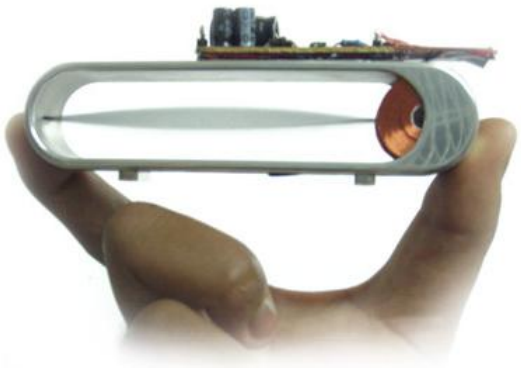

Figure 6: The Micro-Scale Windbelt developed by Shawn Frayne that can power light and temperature sensors [13]

A different design was used in the flutter mill devised by Tang et al., [14] in 2009. A cantilevered flexible web was suspended by springs to flutter in axial fluid flow. An electromagnetic method was used to harvest the energy generated by fixing a conductor circuit on the web and fixing it between magnetic panels as shown in Figure 7.

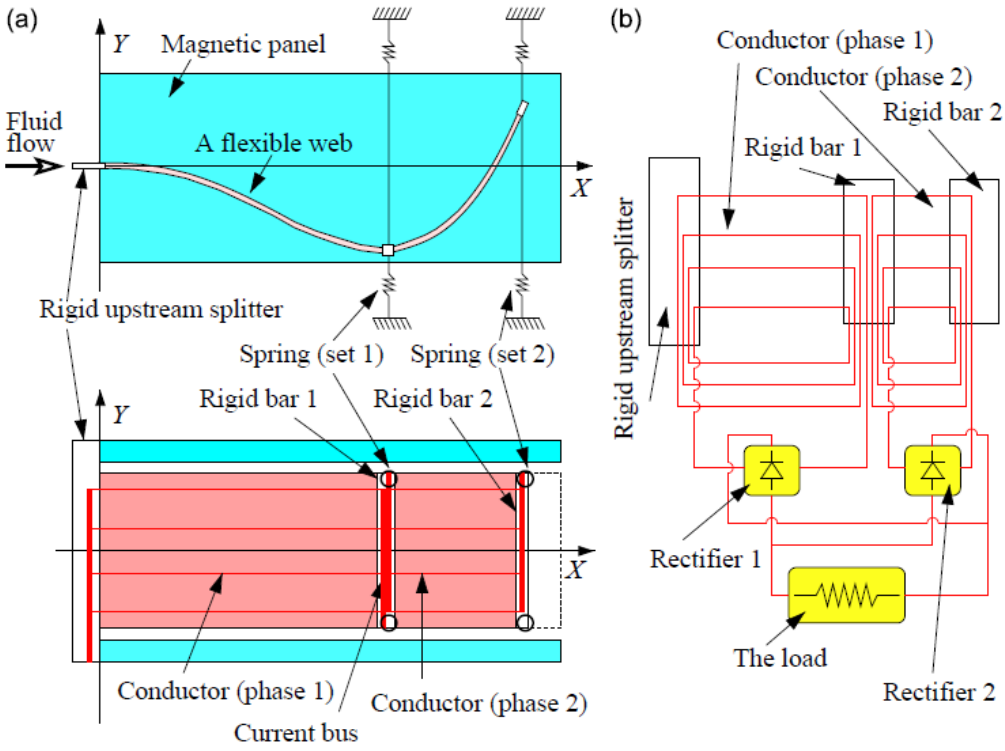

Figure 7: The design of the flutter-mill devised by Tang et al., [14]

In 2009, Zhu et al., [15] devised a different model of a flow energy harvester in which an air foil is subjected to an air stream where the air foil is rotated by an actuator along its axis and is installed on a spring and a damper (Figure 8). They were able to investigate the performance of the system through 2D and 3D numerical models

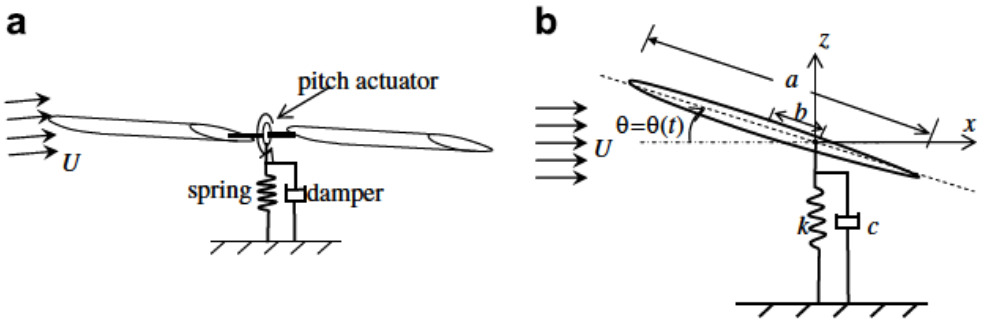

Figure 8: A Schematic of the flapping foil Energy Harvester [16]

In 2009, Barrero-Gil et al., [16] analytically explore the use of one-degree-of-freedom transverse galloping to obtain energy. They established relations between the flow velocity and energy efficiency for air foils of different masses and cross-section geometries.

Jung et al., [17], in 2009, used a permanent magnet and a coil to harvest the wake galloping of a spring supported cylinder subjected to an air stream as shown in Figure 9. They carried out wind tunnel tests to verify the effectiveness of their proposed device.

In 2011, Bibo et al., [18] devised a micro wind power generator for which they developed a nonlinear single mode model and verified its results experimentally. They embedded a piezoelectric beam at the end of a cavity that is subjected to a wind stream. As the wind blows the beam vibrates mimicking the oscillations of the reeds of music-playing harmonica (as shown in Figure 10).

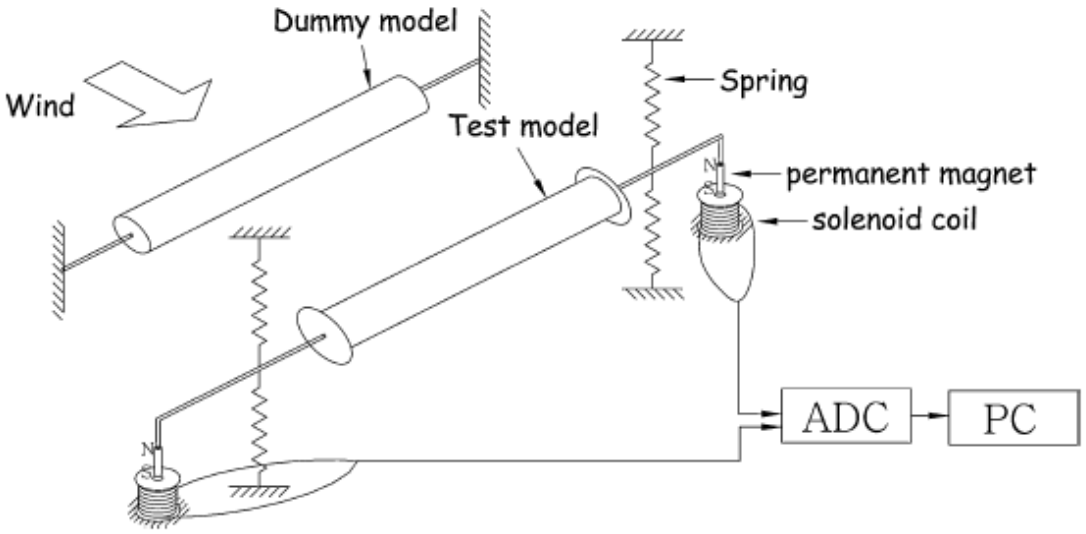

Figure 9: The experimental setup used by Jung et al., [17]

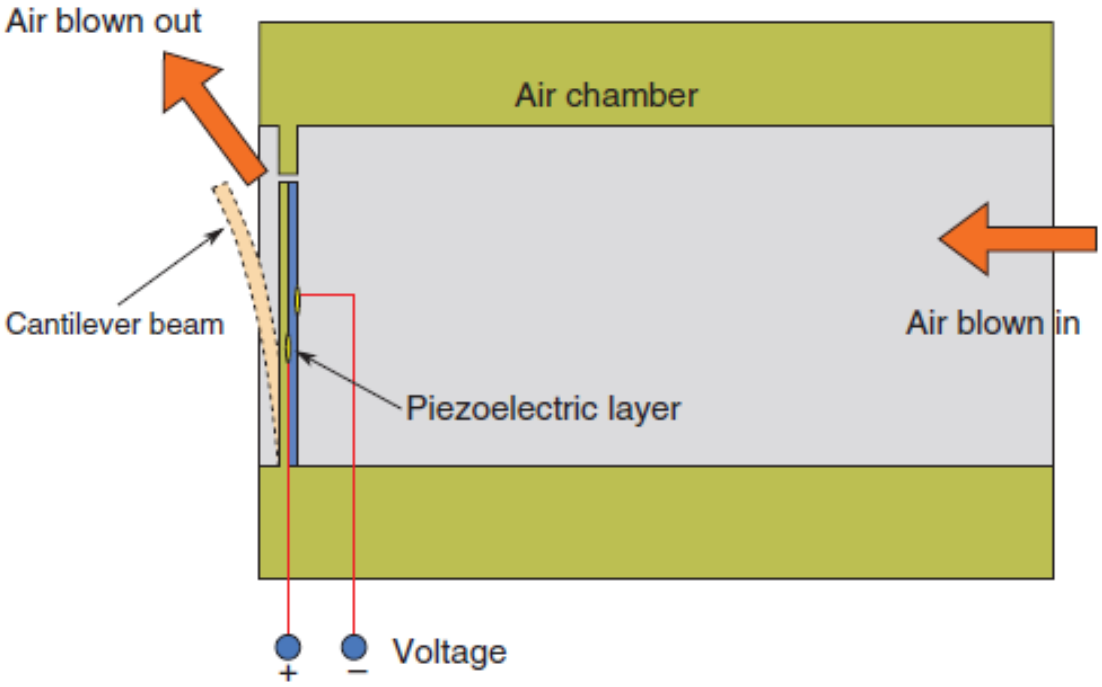

Figure 10: Operation Concept of the Micro-Power Generator devised by Bibo et al., [18]

Also in 2011, Sirohi and Mahadik [19] proposed a devise that consists of cantilever beams with their ends attached to a triangular cross section that is subjected to a wind stream. They bonded piezoelectric sheets to the beams to generate electrical energy (Figure 11). They fabricated and tested their device and were able to generate up to 53 mW which was enough for their intended purpose of powering low-power sensors.

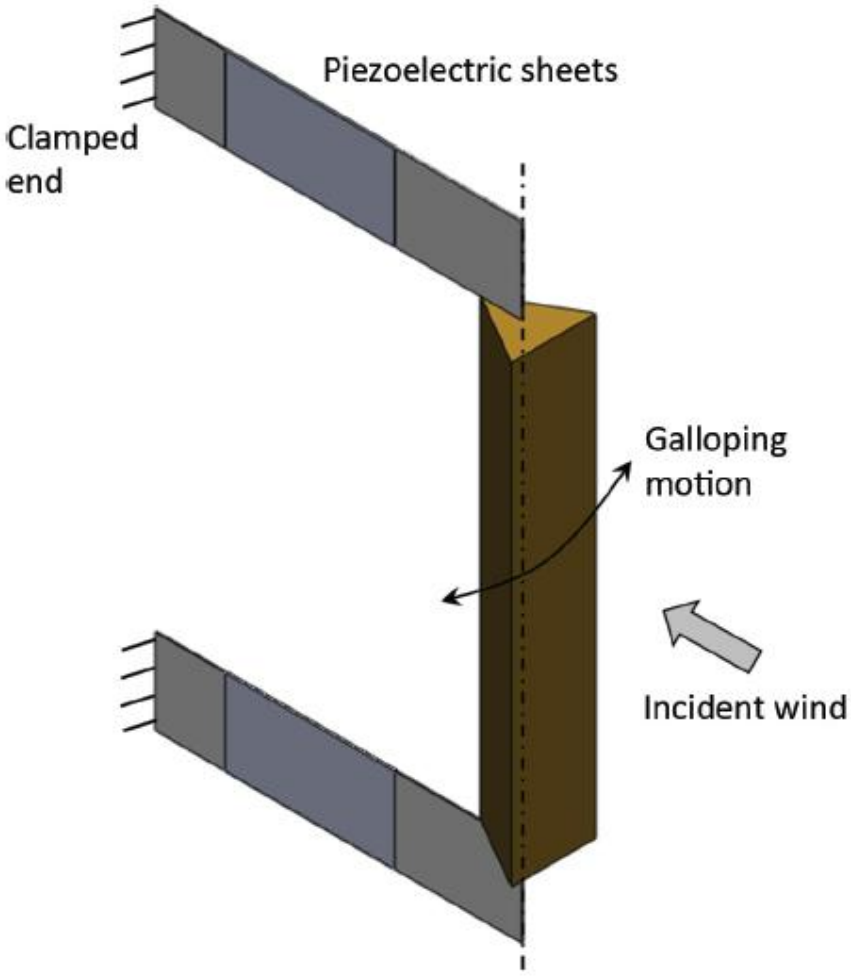

Figure 11: Galloping Energy harvester devised by Sirohi and Mahadik [19]

1.6 Aerodynamic Instability Phenomena

Most of the devises described in the previous section as well as the devise proposed in this thesis rely on aerodynamic instability phenomena. These phenomena have been historically studied by civil and aerospace engineers as undesirable phenomena that should be studied and avoided when designing bridges, high tension suspended power cables, and airplane wings. Figure 12 shows the case of the collapse of Tacoma Narrows bridge which collapsed in 1940 causing civil engineers around the world to further investigate the causes of flutter and consider it while designing suspension bridges [20].

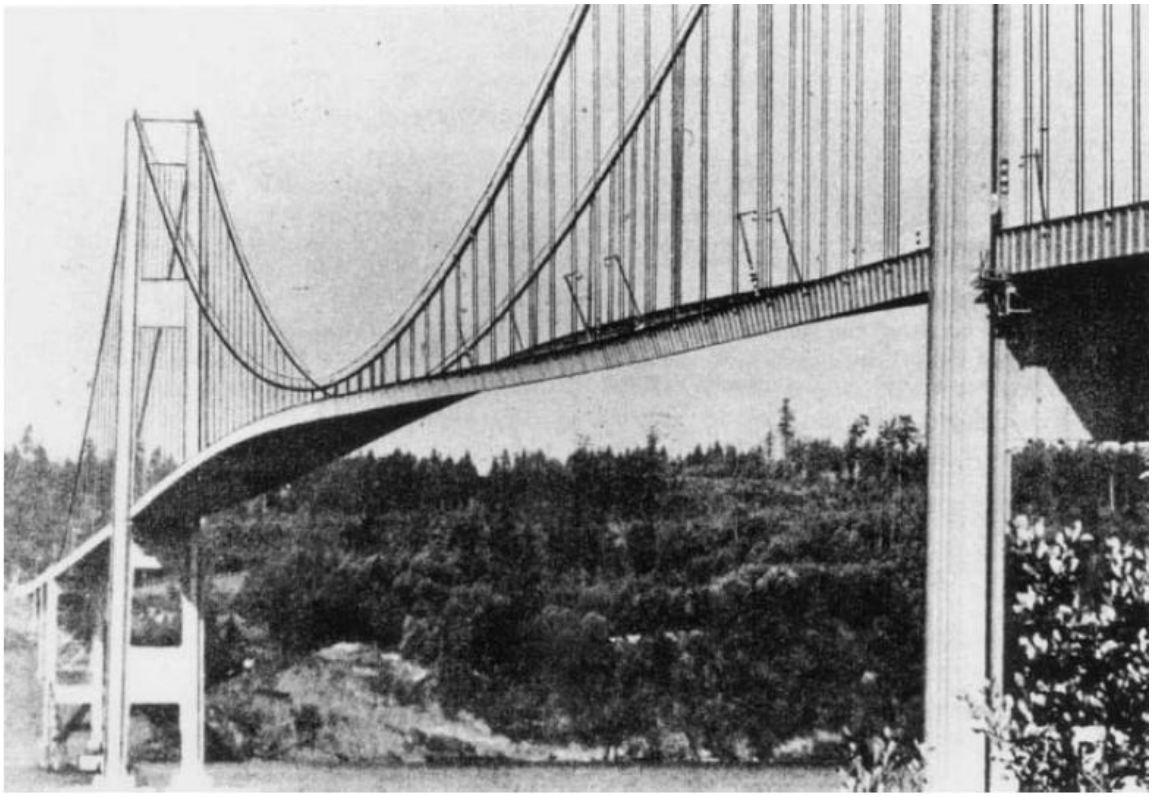

Figure 12: The flutter of Tacoma Narrows Bridge before its collapse [20]

These Phenomena include vortex induced vibrations, wake galloping, buffeting and divergent oscillations. Figure 13 shows the variation of the vibration amplitude with the increase of wind velocity for each case [21].

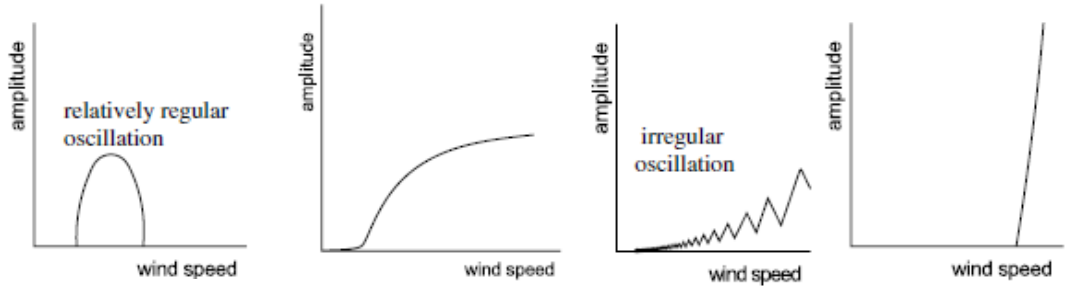

(a) Vortex-induced vibration (b) Wake galloping (c) Buffeting (d) Divergent oscillations

Figure 13: A comparison between amplitude variation with velocity curves of different aerodynamic instability phenomena adopted from Jung and Lee [21]

Vortex induced vibrations are associated with periodic lift forces caused by vortex shedding that may occur at a specific range of wind speeds for which the exciting frequency is close to the natural frequency of the vibrating body. The resulting vibrations will depend on Reynold's number, and the turbulence of the incoming wind near the boundary layer of the vibrating body as explained by Dowell [22].

Wake galloping the phenomenon upon which Jung et al., [17] relied when setting up the design for their devise as previously shown in Figure 9 relies on a vortex that is generated when wind passes by a stationary obstacle forming behind it what is known as Kármán vortex trail. This vortex trail, as explained by Den Hartog [23], consists of pattern of consecutive clockwise and counterclockwise vortices that can cause vibrations in bodies placed downstream. This phenomenon was originally noted and studied for multiple stacked cables in suspended power transmission lines.

Buffeting vibrations are vibrations associated with randomly generated fluctuating forces that occur due the turbulent flow as explained by Dowell [22]. This phenomenon is widely studied for designing wind resistant structured. However it does not offer a stable force of vibration for energy harvesting.

Divergent oscillations, such as galloping of power transmission cables with snow formation and flutter of aircraft wings, are aero-elastic instabilities that cause the vibrations to self initiate at a certain threshold of wind velocity. When this threshold is exceeded the amplitude of the oscillations are directly correlated with the increase in wind speed as shown in Figure 13 [21].

The term "aero-elastic galloping" is historically used by civil engineers for fluid forces that occur due to an angle between the wind direction and the resulting force due to nonsymmetrical cross sections of certain slender shapes can result in negative damping that causes a single degree of freedom instability as explained by Den Hartog [23].

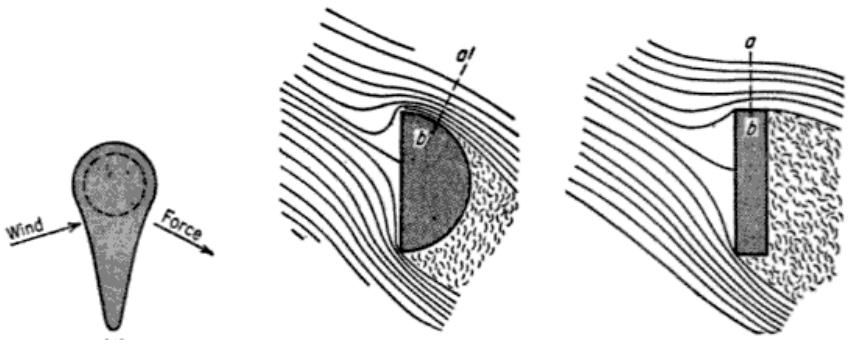

Figure 14: The slender cross sections for which resulting wind force directions cause galloping [23]

Aero-elastic flutter is another type of divergent oscillations that is defined as the coupled torsion-plunge instability of a structure due to the forces induced by fluid flow.

This phenomenon has been thoroughly studied by aerospace engineers trying to avoid its damaging effect on airfoil structures [24]. Both the lift force and the pitching moment will be dependent on the velocity of the body, so they will be subtracted from the system's damping. If the total damping term becomes negative, which means that more energy will be pumped into the system, vibrations will be initiated [22].

1.7 Research Objectives

The objective of the present research is to address the key concept of generating mechanical vibration from fluid flow, and exploiting the ensuing motion to harvest useful energy. The work is motivated by the continual worldwide quest to exploit renewable energy sources through novel means, together with the ubiquity of fluid flow as a clean and sustainable source of energy. While, for many years, the generation of energy from fluid flow has been centered on the use of rotating machinery, the concept presented herein departs radically from the conventional turbine technology. It relies on the development of small, scalable devices that can easily be installed wherever power is needed. In this context, the phenomenon of aero-elastic flutter needs to be exploited, wherein an incoming flow of fluid causes self-sustained oscillations in an elastic structure in contact with the fluid. The ensuing mechanical motion is then converted into useful electric power through an electromagnetic transducer that is integrated with the device. Conceptually the proposed device consists of an elastic cantilever beam that carries a tip mass in the form of a lightweight box having a square cross-section to undergo flutter when placed in a wind stream. A magnet is placed on the beam, and a coil is fixed around it, so when flutter occurs an electric current is induced in the coil. As

such, the device contains few mechanical parts requiring minimal or no maintenance, which makes it an ideal candidate for a power enabler in many applications where the use of other energy sources may be too costly or infeasible. The device is particularly adaptable to provide sustainable energy for remote low-power electronic devices that are placed wherever access to wind flow is available.

Emphasis is placed on studying the system performance at different air speeds while accounting for the design parameters such as the beam length, the square section dimensions, and its respective lift and drag characteristics (which depend on Reynolds' number for the flow [24])in an attempt to formulate a dynamic model to be verified experimentally through wind tunnel testing.

1.8 Thesis Organization

This remainder of this thesis is organized into four chapters. Chapter 2 presents the design of the proposed energy harvester together with the numerical model that is formulated to predict the dynamic performance in terms of the mechanical displacements and output voltage and electric power as a function of the incoming wind characteristics and load resistance. Chapter 3 presents the setup for the experimental wind tunnel tests as well as the procedures followed to complete these tests. Chapter 4 illustrates the experimental results in comparison with the model predicted ones. Finally, Chapter 5 presents conclusions and recommendations for future work.

2 HARVESTER DESIGN AND MODELING

A square section light weight material box is fixed to the free end of a flexible cantilever beam. Due to the air flow the box exhibits rotational and transverse motions which are associated with flutter. Inducing and maintaining this self-excited vibration is pivotal to the design of the wind harvester. Energy can be extracted in a number of ways including electromagnetic and piezoelectric techniques. This chapter presents the finite element model that is developed to study the dynamics of the flutter foil. The treatment is organized in three subsections detailing the mechanical, aero-elastic and electromechanical models.

2.1 Harvester Design

Figure 15 shows a schematic illustration of the proposed design. A lightweight box having a square cross-section is mounted at the tip of a flexible cantilever beam facing an incoming steady wind stream with a mean speed U. Wind-induced vibration causes the box to flutter in the transverse direction, leading to self-excited bending vibrations in the beam. Energy is harvested using a pair of magnets sandwiching the beam that move past stationary coils, as indicated. The time-varying lift and drag forces depend on the relative motion of the structure and the surrounding air and are responsible for the ensuing vibration of the structure. These aerodynamic loads will be studied in the next section.

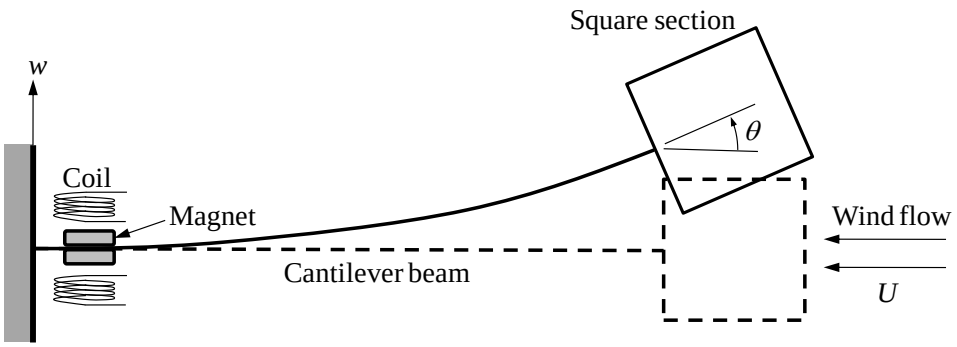

Figure 15: Schematic illustration of proposed design (top view)

2.2 Purpose of the Finite Element Model

A model has been devised in order to investigate the systems performance and predict its response for different wind speeds and system parameters. The model integrates the system's structure with the predicted aerodynamic forces and the effect of the electromechanical system in order to calculate the resulting voltage drop across different resistances attached to the system at different wind speeds.

2.3 Model for the System Structure

The beam was divided into two-node elements subject to both transverse and rotational displacements represented by the odd and even numbered elements in the displacement vector, respectively, as depicted in Figure 16 [25]. The axial loading on the beam was neglected due to relatively small rotation angles.

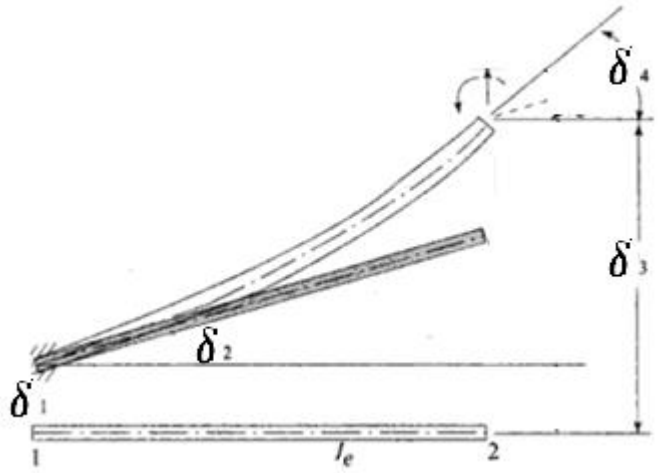

Figure 16: The Deformed configuration of the beam element adopted from [25]

The mass and stiffness matrices were found to be as shown below (refer to Appendix A for their derivation) [25]

$$[M_e] = \frac{\rho A l_e}{420}\begin{bmatrix} 156 & 22l_e & 54 & -13l_e \\ 22l_e & 4{l_e}^2 & 13l_e & -3{l_e}^2 \\ 54 & 13l_e & 156 & -22l_e \\ -13l_e & -3{l_e}^2 & -22l_e & 4{l_e}^2 \end{bmatrix} \quad (1)$$

$$[K_e] = \frac{EI}{{l_e}^3}\begin{bmatrix} 12 & 6l_e & -12 & 6l_e \\ 6l_e & 4{l_e}^2 & -6l_e & 2{l_e}^2 \\ -12 & -6l_e & 12 & -6l_e \\ 6l_e & 2{l_e}^2 & -6l_e & 4{l_e}^2 \end{bmatrix} \quad (2)$$

The mass moment of inertia of the square section box is calculated which will be equal to 1/6 × box mass × squared side width assuming uniformly distributed mass. It will be added along with the box mass to the tip node diagonal elements after assembling the mass matrix. The stiffness and force matrices are also assembled.

The damping matrix is estimated as $[C] = \gamma [M] + \beta [K]$ as it was estimated by De Marqui et al., [26]. This damping term only includes mechanical damping in the system whereas electromagnetic damping will be included later in the force terms. Initial assumptions were made for the values of constants γ and β until an estimate that produces a stable response that provides realistic peak values for the tip displacement that was experimentally verified was settled upon.

2.4 Aero-elastic Model

For spring supported body shown in Figure 17 having Geometrical characteristic b (equals to section width multiplied by the body length) subjected to a steady flow of velocity U and fluid density ρ_{air}, where θ is the angle of inclination of the square section and α is the angle between the flow velocity and relative velocity of the wind U_{rel} to the square section moving at a velocity $\dot{w}$ the steady fluid dynamic forces per unit length will be: [24, 27]

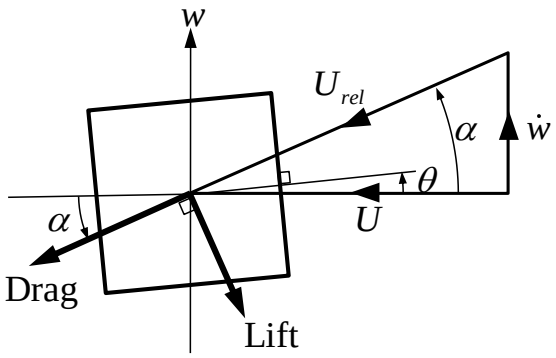

Figure 17: Air loads acting on square section

$$L = \frac{1}{2}\rho_{air} U_{rel}^2 b C_L|_{\alpha-\vartheta} \qquad (3)$$

$$D = \frac{1}{2}\rho_{air} U_{rel}^2 b C_D|_{\alpha-\vartheta} \quad (4)$$

where D & L are the drag and lift force that are by definition the force in the direction of the relative velocity of the wind and the force perpendicular to it. C_L and C_D are the lift and drag coefficients which are dimensionless coefficients for which there are readily available experimentally obtained curves for the different cross sections. These coefficients are evaluated at an angle equal to the difference between the section inclination and the relative wind velocity.

From geometry, we note:

$$U_{rel} \cos\alpha = U \quad (5)$$

Resolving the forces along the transverse direction gives:

$$F_A = -D \sin\alpha - L \cos\alpha \quad (6)$$

which can be written as:

$$F_A = \frac{1}{2}\rho_{air} U^2 b \sec^2\alpha \left(-C_D|_{\alpha-\vartheta} \sin\alpha - C_L|_{\alpha-\vartheta} \cos\alpha\right) \quad (7)$$

where

$$\alpha = \tan^{-1}\left(\frac{\dot{w}}{U}\right) \quad (8)$$

The lift and drag coefficients that are present in equations 3 and 4 are highly dependent on the section geometry, as well as the flow characteristics, mainly Reynolds number. Different studies have been made to investigate the variation of the lift and drag coefficients with the angle of attack for rectangular sections; however their study was

limited to small angles of attack [28, 29]. Mukhopadhyay et al., [27] experimentally obtained values for the lift and drag coefficients for the square section at different values for Reynolds number. At Reynolds number of 2700 the lift and drag coefficients were found to vary with the angle of attack as depicted in Figure 18. Ignoring the wind effect on the beam and the moment on the square section the force vector will be reduced to a point force at the tip of the beam.

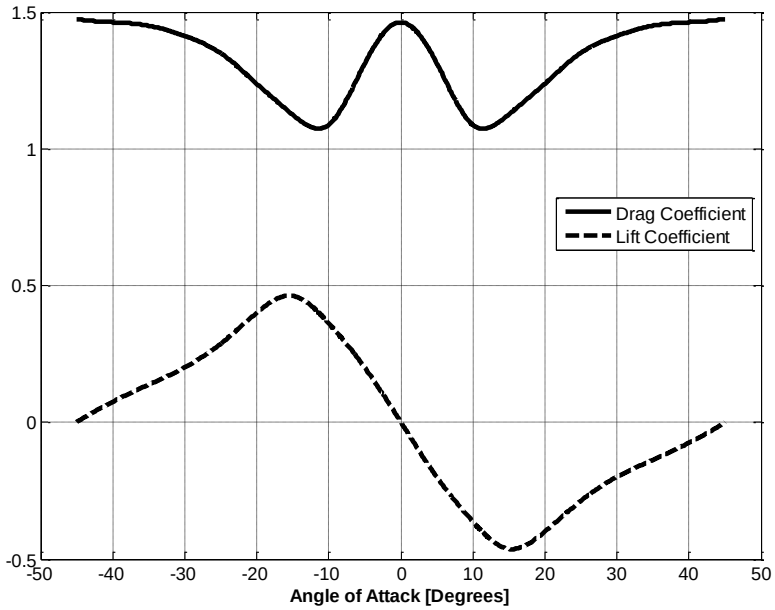

Figure 18: Variation in lift and drag coefficients with time [27]

2.5 Electromagnetic Model

In 2004 Poulin et al., [30] presented a model for the effect of inducing current electromechanically using a magnet and a coil on a system having a single degree of freedom system where there is only a linear motion of the magnet in the direction of the coil axis of the coil. The magnet was found to act on the system with a force proportional to the induced current, and the induced current is proportional to the magnet velocity as

given by the equations below. Since the magnet in our devised system is placed near the fixed end where the angle of rotary action can be neglected, the same equation can apply [30].

$$V = Bl_w \frac{d\delta_n}{dt} - R_c i - L_c \frac{di}{dt} \quad (9)$$

$$i = \left(\frac{1}{R_l + R_c}\right)\left(Bl_w \frac{d\delta_n}{dt} - L_c \frac{di}{dt}\right) \quad (10)$$

Where n is the node at which the magnet is placed, B is the magnetic flux density, l_w is the wire length of the coil, i is the electric current, V is the voltage drop across the load resistance, R_l is the load resistance, R_c is the coil resistance, and L_c is the coil inductance. Note that the electromagnetic damping term, which is the term multiplied by the node velocity, is included in the calculation of the current which is in turn used to calculate the force.

We add the magnet mass m to the node at which the magnet is place at the diagonal of the mass matrix and the mass moment of inertia to the diagonal element of the following row. The magnet force is added to the corresponding line in the force vector and assuming that the magnet is on the side of the beam a moment term is added to the following element in the force vector.

The added force will be:

$$F_n = -Bl_w i \quad (11)$$

The magnetic flux density was estimated for the average distance between the magnet and the coil using a color coded graphical plot available on the magnet supplier's website. The number of turns of the coil needed to calculate the wire length and the coil

inductance was estimated based on the dimensions of the coil and the measured wire diameter using the equations used by Poulin et al., [30].

$$N = \frac{h_b(D_o - D_i)}{2{D_{Cu}}^2} \tag{12}$$

$$l_w = \frac{\pi N(D_o + D_i)}{2} \tag{13}$$

$$L_C = \frac{\mu_0 N^2 \pi (D_o + D_i)^2}{16 h_b} \tag{14}$$

A check can be made to verify the used values for the wire length and the wire diameter by measuring the coil resistance and comparing it to the resistance that can be calculated using the following equation from Poulin et al., [30].

$$R_C = \frac{4\rho_{cu} l_w}{\pi {D_{Cu}}^2} \tag{15}$$

The resulting electric power can be calculated for a given load resistance at each value of the electrical current using the following equation.

$$P = i^2 R_l \tag{16}$$

2.6 Governing Equations

The element equations of motion are then solved by using Lagrange's solution for ordinary differential equations. Upon assembly, the equations of motion for the flutter foil are expressed as:

$$[M]\{\ddot{\delta}\} + [C]\{\dot{\delta}\} + [K]\{\delta\} = \{F\} \tag{17}$$

Where F is the force vector containing only two transverse forces (the aero-elastic force at the tip and the electromagnetic force at the magnet location nod) and $\boldsymbol{\delta}$ is a vector containing the node displacement and rotations as follows.

$$\{\delta\} = \begin{Bmatrix} w_1 \\ \theta_1 \\ w_2 \\ \theta_2 \\ \vdots \\ w_N \\ \theta_N \end{Bmatrix} \qquad \{F\} = \begin{Bmatrix} 0 \\ 0 \\ \vdots \\ F_n \\ 0 \\ \vdots \\ F_A \\ 0 \end{Bmatrix}$$

The system's governing equations are then reduced to first order ordinary differential equations in preparation for a numerical solution. They will become as follows:

$$\{\dot{v}\} = [M]^{-1}\left(\{F\} - [C]\{\dot{\delta}\} - [K]\{\delta\}\right) \tag{18}$$

$$\{\dot{\delta}\} = \{v\} \tag{19}$$

$$\frac{di}{dt} = (-i(R_l + R_c) + Bl_w v_n)/L_c \tag{20}$$

These equations were solved using multistep numerical formulas and time responses were obtained. An initial condition was used the beam nodes were all assumed to have zero displacement and velocities that are proportional to the beam's static deflection (nodes closer to the fixed end are assumed to have lower velocity than nodes closer to the free end). The beam was divided into 22 elements with the magnet placed at the second element. Figure 19 shows a flowchart of the used model methodology.

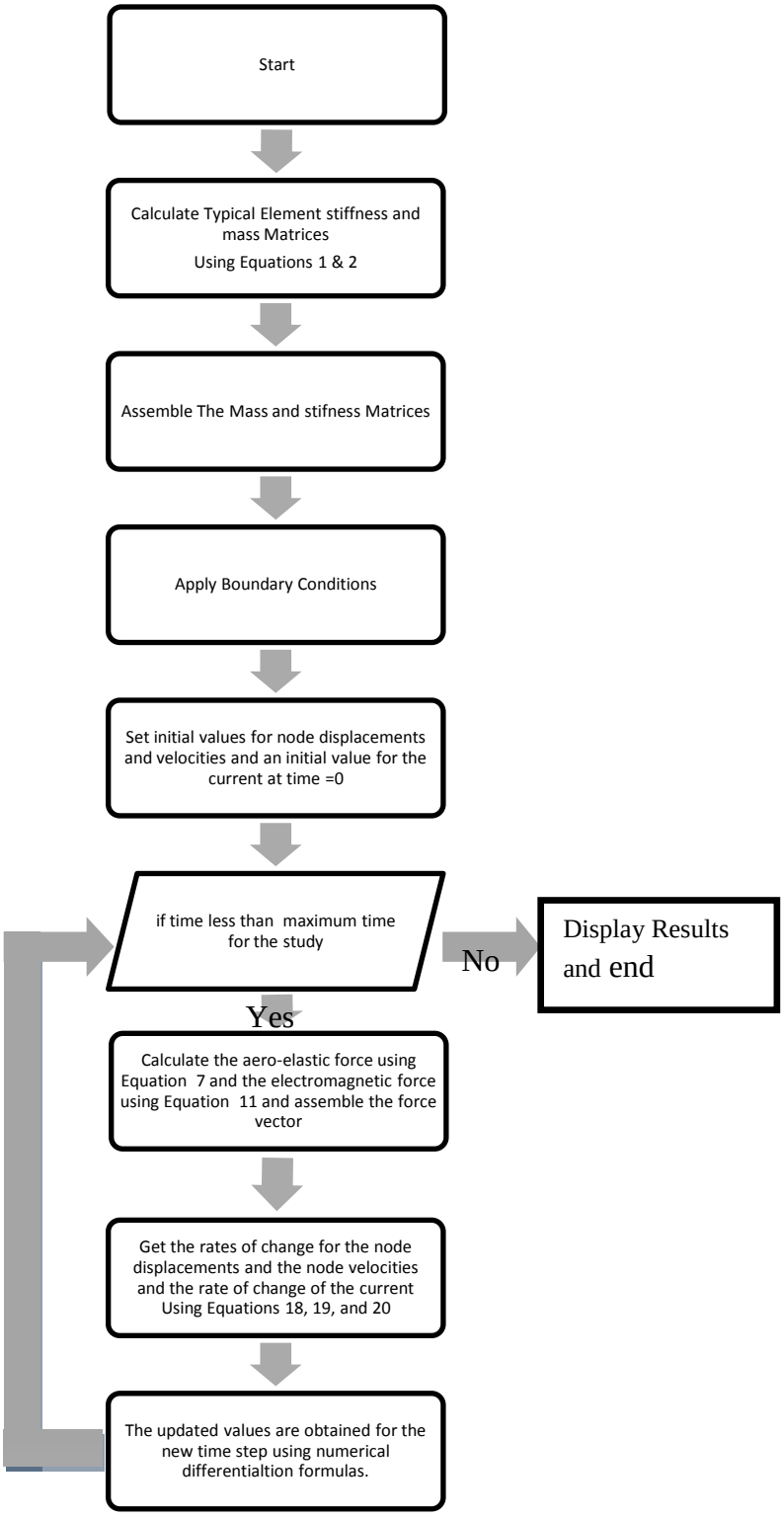

Figure 19: A flowchart for the solution process of the numerical model

3 EXPERIMENTAL WORK

An experiment was set in order to compare the proposed analytical model with the actual results that can be attained. In the following section the experiment done will be thoroughly explained.

3.1 Experimental Setup

As shown in Figure 20, a stainless-steel beam (0.45 mm thick 25 mm wide and 300 mm long) is fixed on a bracket from one end using a bolt, nut and a washer. A light-weight square sectioned end made of paper stiffened with cardboard is attached to the other side of the beam. An NdFeB Grade N42 ring magnet (6.35 mm inner diameter, 12.7 mm outer diameter and 12.7 mm thickness) is attached to the stainless-steel beam 30 mm away from the fixed end and a coil is fixed in front of it. This entire setup is inserted

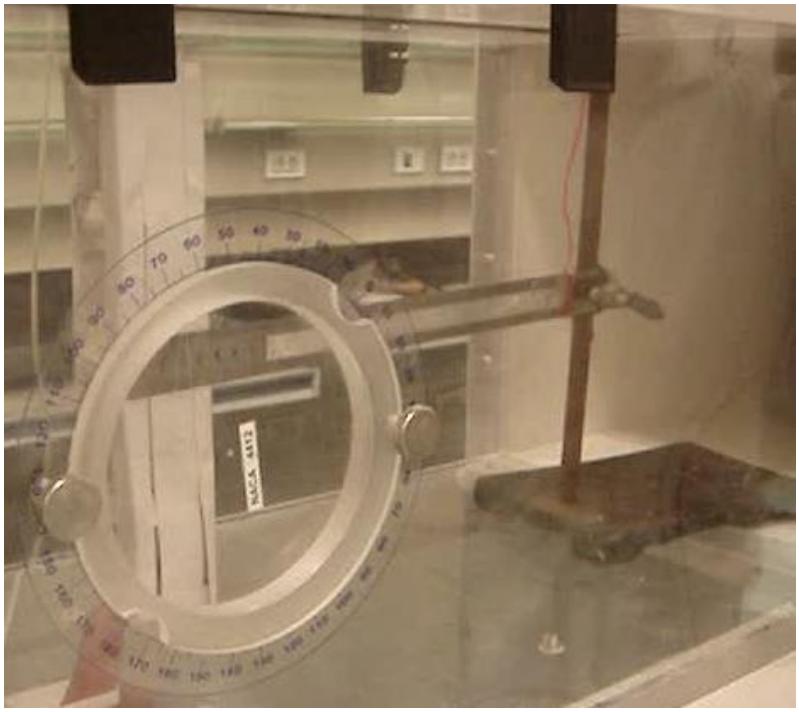

Figure 20 Experimental Setup

into a wind tunnel with a variable frequency drive. The coil ends are then connected by a wire to a variable resistance (resistance decade box). A data acquisition/analyzer (LMS Pimento) is connected in parallel with the variable resistance. This analyzer is connected to a laptop for real-time reading of the transient volt generated by the system. A handheld metal vane anemometer was used to verify the wind speed at each frequency set for the wind tunnel drive. The table below shows the properties of the used materials.

Table 1: Properties used for the experimental results

Square section		
Mass	27	g
Width	5	cm
Length	30	cm
Beam		
Modulus of Elasticity (E)	207	Gpa
Density (ρ)	7800	kg/m^3
Thickness	0.45	mm
Width	25.4	mm
Beam Length (l)	30	cm
Mechanical damping		
Assumed mass matrix coefficient (γ)	0	rad/s
Assumed stiffness matrix coefficient (β)	10^{-5}	s/rad
Air Properties		
Air density (ρ_{air})	1	kg/m^3
Air permeability (μ_0)	$4\pi \times 10^{-7}$	V s /(Am)
Electromagnetic system		
Magnetic flux density at average gap (B)	0.045	tesla
Coil length (h_b)	7	mm
Coil outer diameter (D_o)	12	mm
Coil inner diameter (D_i)	4.5	mm
Coil wire diameter (D_{cu})	0.11	mm
Coil wire resistivity (ρ_{cu})	17×10^{-9}	Ωm

3.2 Experimental Procedure

The wind tunnel was operated at three different wind speeds. For each run the resistance decade box is set to the required resistance, and the square sectioned airfoil is set to start from rest. Forty seconds are recorded using the analyzer software for each run to insure that the system is passed the transient phase and the vibrations that it has definitely reached a steady state. Five runs were made for every wind tunnel frequency to reach a total of fifteen runs.

4 RESULTS

4.1 Transient Response comparisons

The experiment was performed over a resistance range of 40 Ω to 4 MΩ and the transient voltage was recorded for different wind speeds. The transient peaks are observed to grow until they reach a steady state. An oscillatory behavior for the steady state peaks for the experimental results is noted which may be caused by some turbulence in the air stream. The top part of Figure 21 shows the transient voltage response as predicted by the model for 100Ω resistance at 3.2 m/s wind speed as an example. Appendix B provides similar figures for all the other experimental runs. The model predicted system responses in all cases appear to be closely matched by the experimentally recorded outcome for their cases; however the oscillatory components seem to be diminished.

4.2 Frequency Comparisons

The model predicted frequency for all the model runs made is about 1.9 Hz which is the natural frequency of the system that was not noticeably affected by adding the electromagnetic effect at any load resistance or by changing the wind speed. The experimentally measured dominating first mode frequency was around 1.7 Hz that did not change noticeably for any of the runs either.

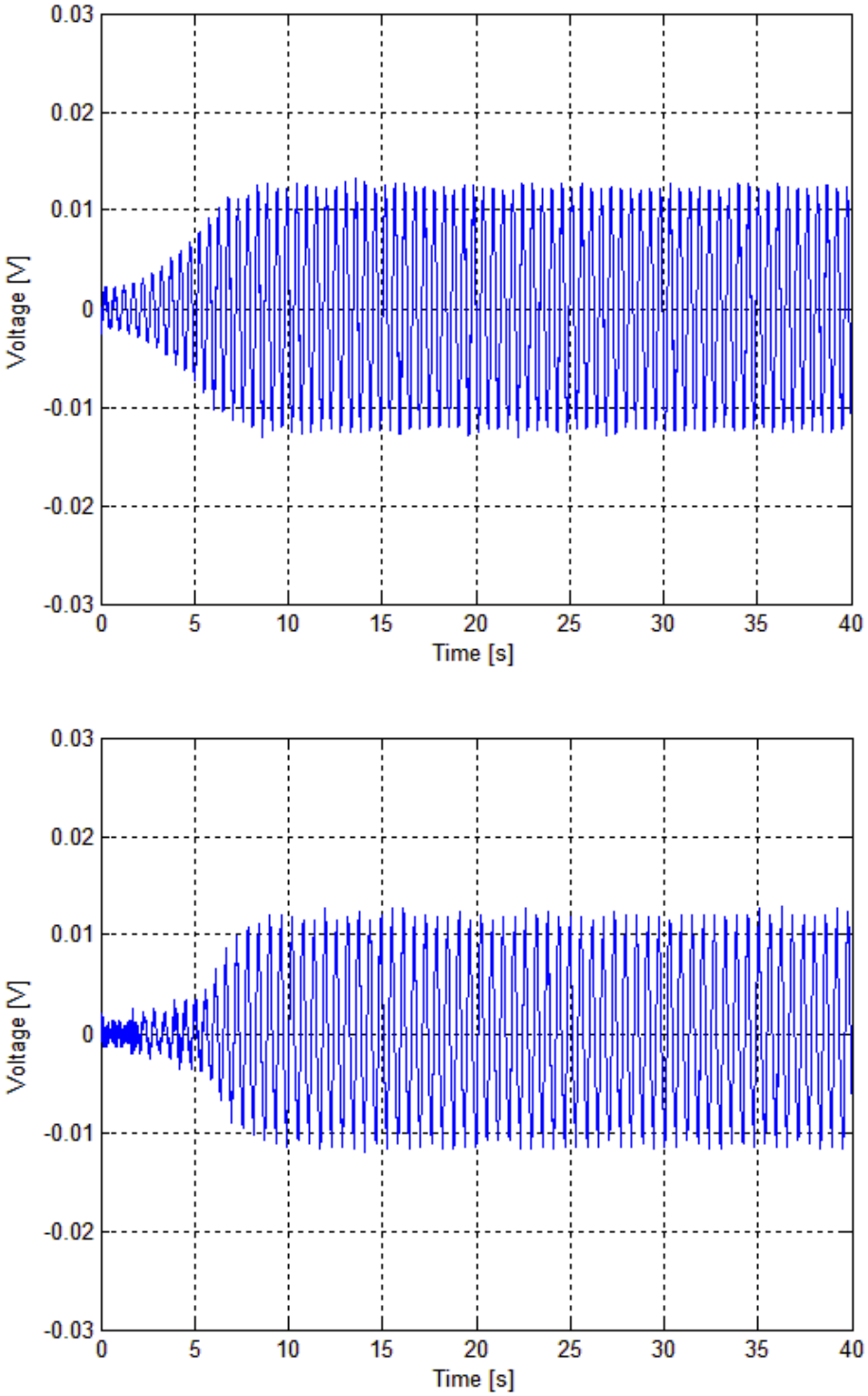

Figure 21: On top is the model predicted time response for the system using 100 ohm resistance at the wind speed of 3.2 m/s and below it is the experimentally measured response for it

4.3 Voltage and Power Comparisons at Steady State

The maximum achieved power for the three experimentally measured wind speeds of were found to occur at 100 Ω resistance and the model predicted power peak value was found to be at approximately the same value for the load (Figure 22, Figure 23, and Figure 24). The output power was predicted to be directly proportional to the wind speed which was verified by the experimental results. With the magnet and coil used the maximum power achieved for a single magnet and coil was around 1.7 μW. The model was capable of predicting the increasing power trend with the load resistance until the peak then the decrease that occurs for higher values of load resistance.

4.4 Tip Displacement and Tip Rotation

Although tip displacement and rotation were not accurately measured in the lab, the amplitudes predicted by the model visually match what was noticed in the experimental runs. It was also found out that the force applied by the electro-magnetic system on the model did not have much effect on the structural Dynamics of the system (Figure 25 and Figure 26)

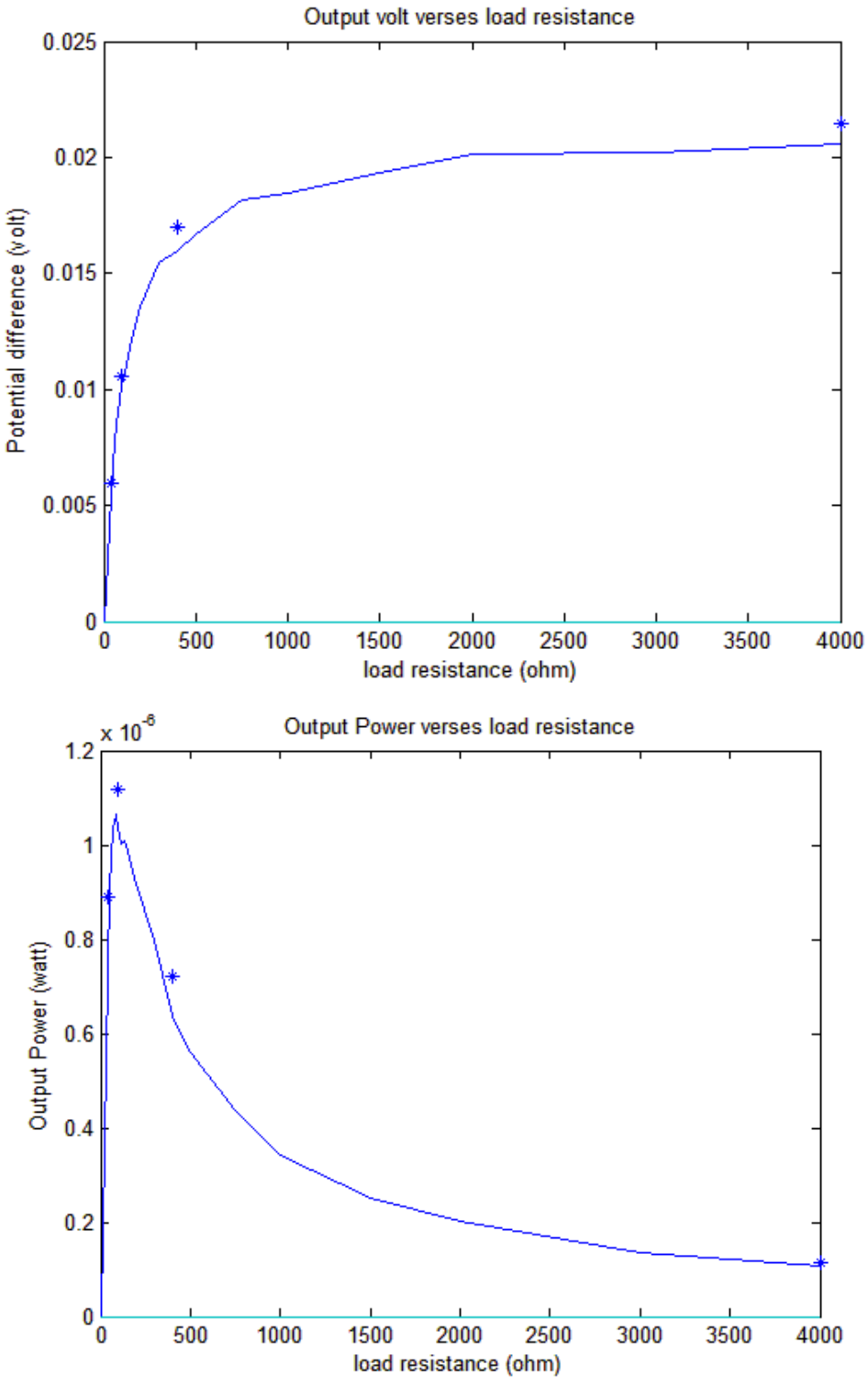

*Figure 22: Graphs showing the correlation between the experimental (denoted by *) and the model predictted values (denoted bu (-) for the volt (in the top drawing) and the power (in the bottom drawing) for different values of load resistance for wind speed of 2.3 m/s*

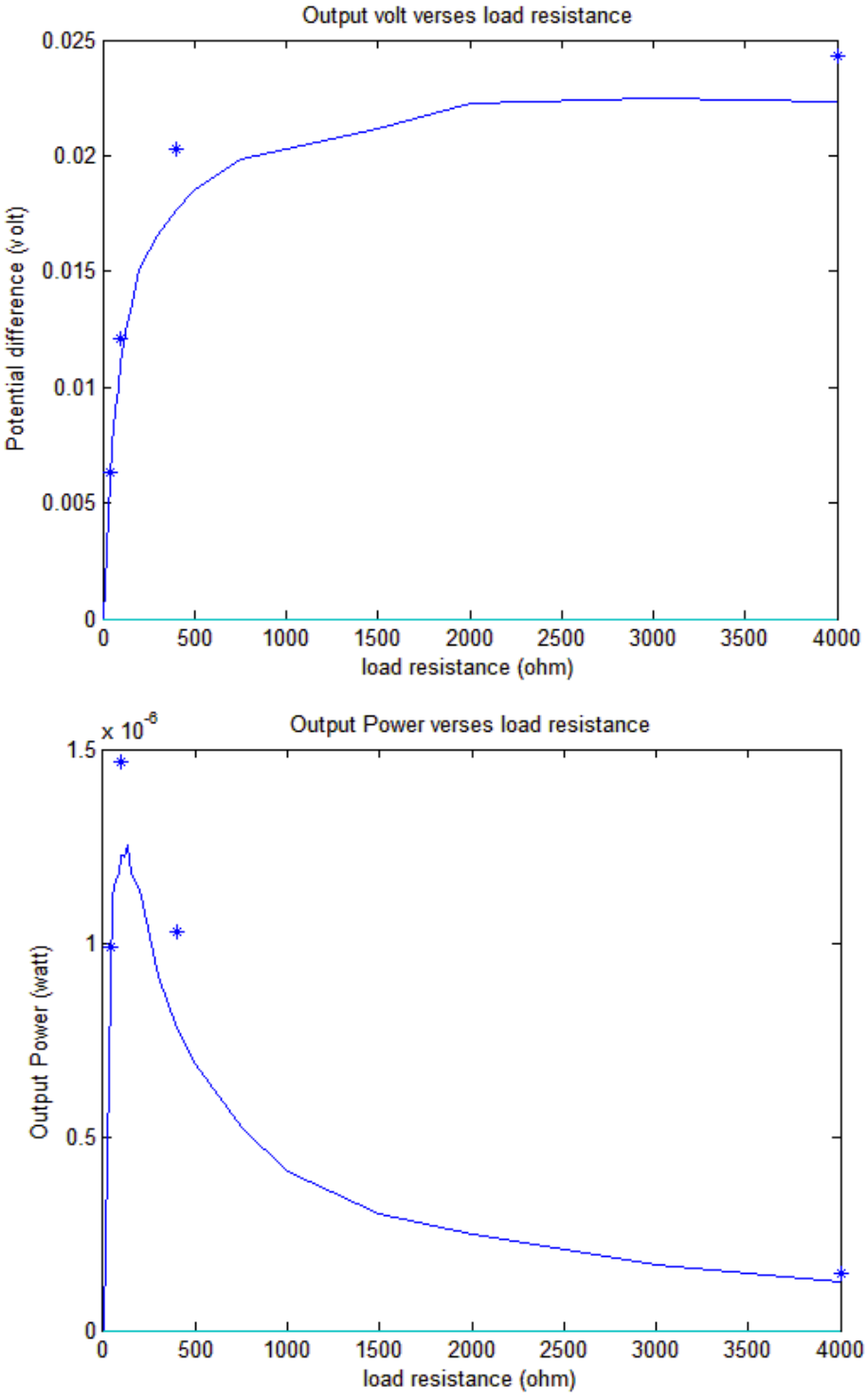

*Figure 23: Graphs showing the correlation between the experimental (denoted by *) and the model predictted values (denoted bu (-) for the volt (in the top drawing) and the power (in the bottom drawing) for different values of load resistance for wind speed of 2.7 m/s*

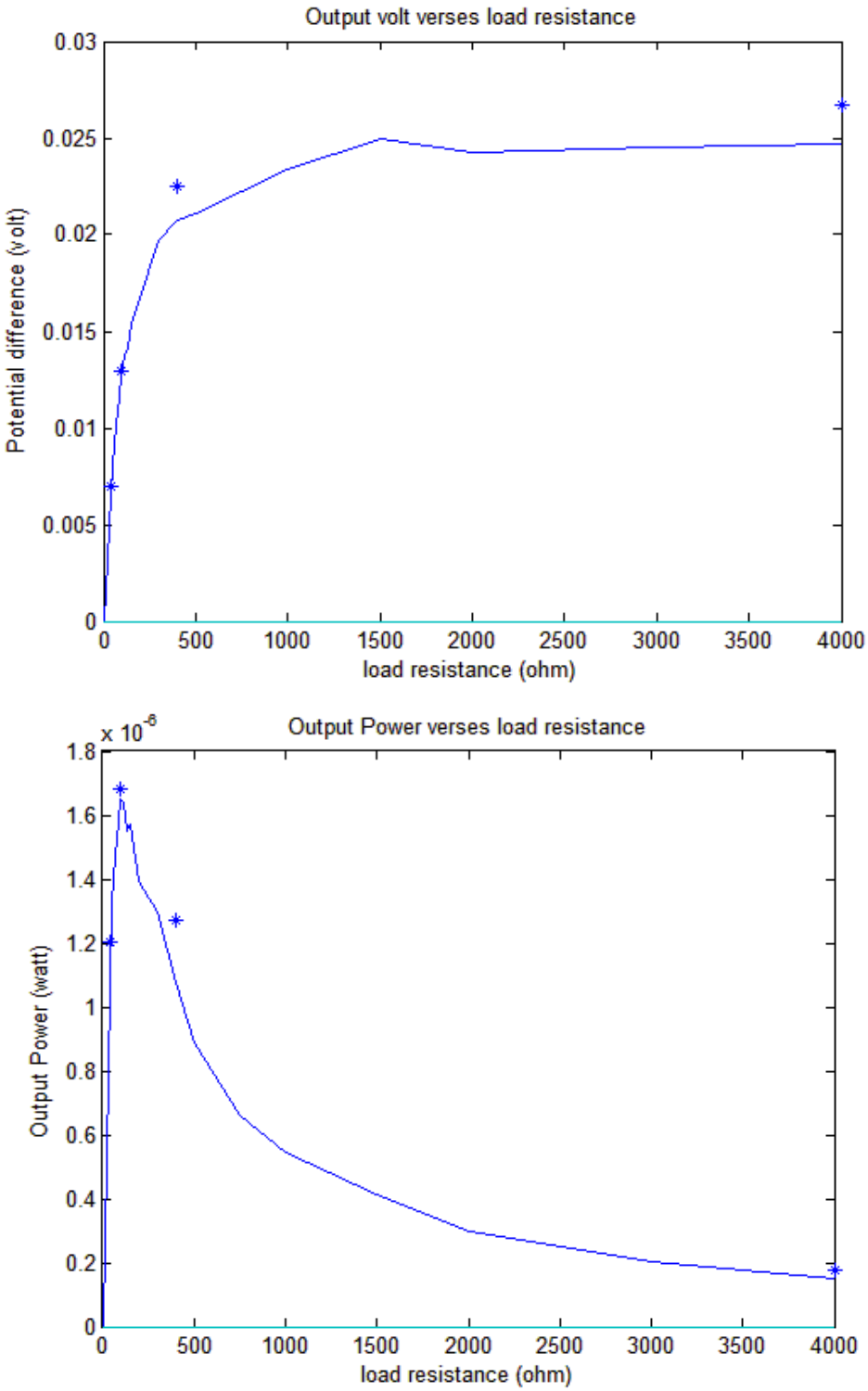

Figure 24: Graphs showing the correlation between the experimental (denoted by *) and the model predictted values (denoted bu (-) for the volt (in the top drawing) and the power (in the bottom drawing) for different values of load resistance for wind speed of 3.2 m/s

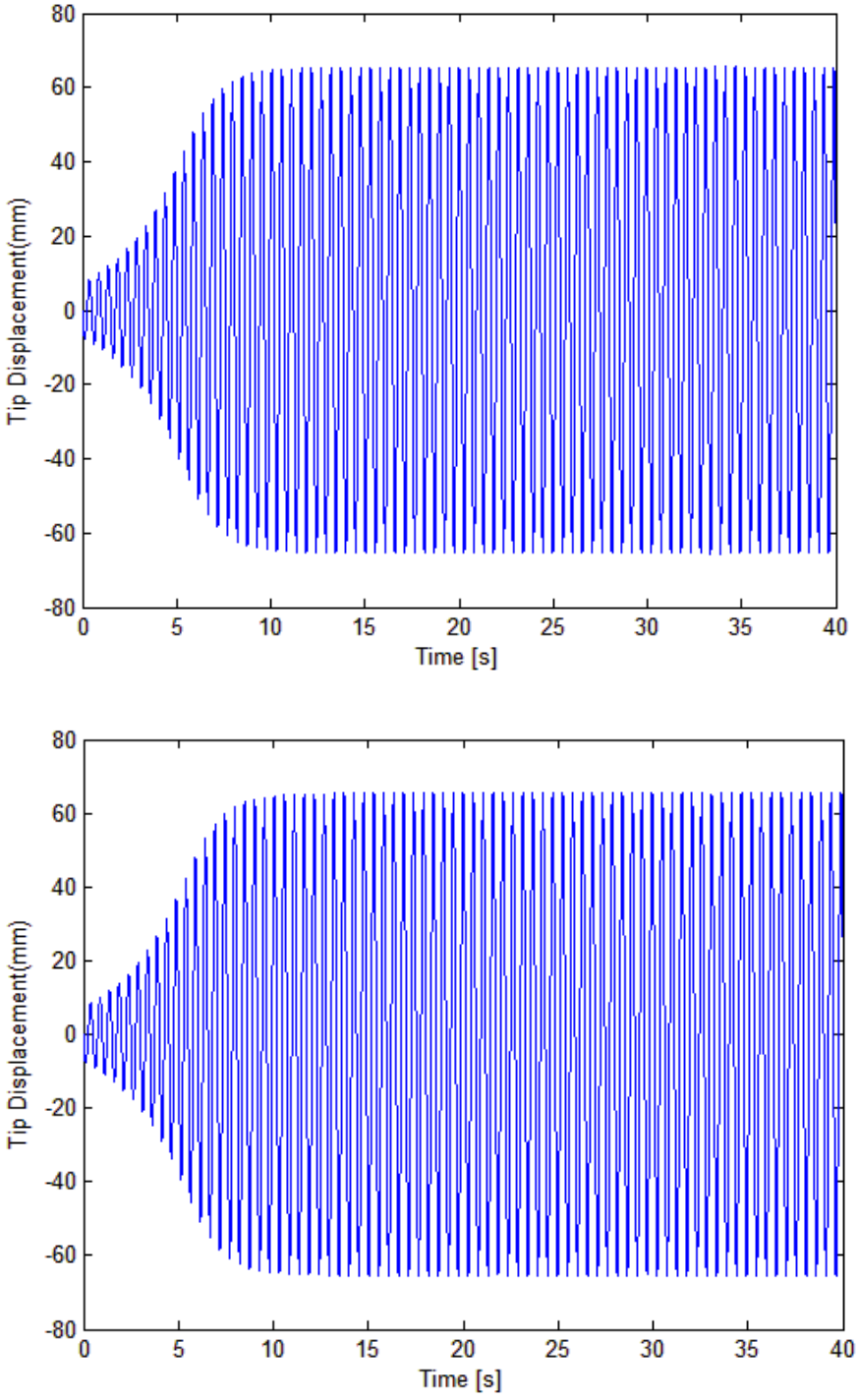

Figure 25: Model predicted tip displacement time plots where the electromagnetic effect and the magnet mass are removed and they are present in the bottom drawing

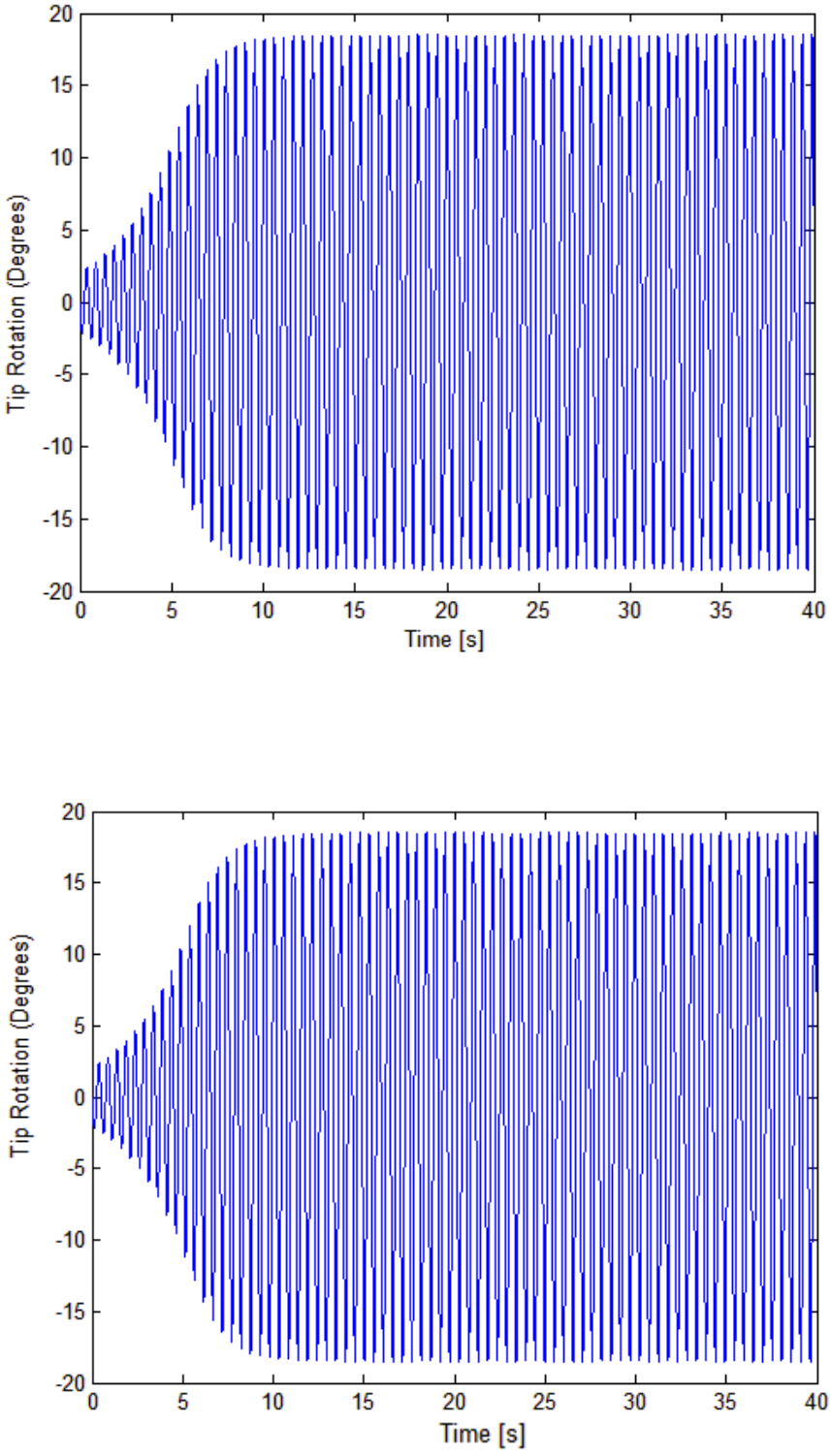

Figure 26: Model predicted tip displacement time plots where the electromagnetic effect and the magnet mass are removed and they are present in the bottom drawing

5 CONCLUSIONS

In this study, a new small-scale wind energy harvester was devised, modeled and experimentally verified. The model was achieved by analytically formulating a set of ordinary differential equations that complement the mechanical model of the beam with the aero-elastic flutter of the square section at the tip and the electromagnetic effect of the energy harvesting coil. These ordinary differential equations were numerically solved for an adequate time span to insure a steady state is reached. Wind tunnel experiments were carried out for different wind speeds and electric loads that would allow proper representation of the power and voltage plots, and the model was found to predict the system's behavior very well.

This system converts kinetic energy into electrical energy using a very economical setup that can be used to supply wireless sensors providing an echo-friendly alternative to alkaline batteries that are used once and land-filled. This system is very simple and can result in great savings in battery costs and can be a good solution to power sensors that are not accessible for battery change.

The maximum achieved power for the used model at 5 m/s wind speed was 1.7 μW which is relatively low. However, this system can still undergo many improvements. The used electromagnetic damping, and magnet mass do not have any noticeable effect on the system dynamics which allows the use of multiple magnets and coils which can, in turn, significantly increase the power output. Piezoelectric materials can be also used to supply additional power. Moreover, additional work can be made to optimize the system

using more powerful magnets and coils which was not the focus of this study. Using the devised model can also help optimize all the system parameters such as the beam, and square end dimensions. However, optimizing the magnet location may need more effort in estimating the average magnetic flux for each case.

REFERENCES

[1] C. R. Saha, T. O'Donnell, H. Loder, S. Beeby and J. Tudor, "Optimization of an Electromagnetic Energy Harvesting Device," *IEEE Transactions on Magnetics 42,* vol. 10, pp. 3509-3511, 2006.

[2] S. Roundy and P. K. Wright, "A Piezoelectric Vibration Based Generator for Wireless Electronics," *Smart Materials and Structures,* vol. 13, pp. 1131-1142, 2004.

[3] P. D. Mitcheson, T. C. Green, E. M. Yeatman and A. S. Holmes, "Architectures for Vibration-Driven Micropower Generators," *Journal of Microelectromechanical Systems,* vol. 13, no. 3, pp. 429-440, June 2004.

[4] V. R. Challa, M. G. Prasad, Y. Shi and F. T. Fisher, "Evaluation of Coupled Piezoelectric and Electromagnetic Technique for Vibration Energy Harvesting," *Proceedings of the SPIE,* vol. 6935, 2008.

[5] M. A. Rabah, M. A. Barakat and Y. S. Mahrous, "Recovering Metal Values Hydrometallurgically from Spent Dry Battery Cells," *Journal of the Minerals, Metals and Materials Society JOM,* vol. 51, no. 12, pp. 41-43, December 1999.

[6] M. F. Almeida, S. M. Xara, J. Delgado and a. C. A. Costa, "Characterization of Spent AA Household Alkaline Batteries," vol. 26, no. 5, pp. 466-476, 16 June 2005.

[7] S. M. Frayne, "Generator Utilizing Fluid-Induced Oscilations". United States of America Patent US2008129254, 5 June 2008.

[8] D. Pike, "Rotor Power Ousts the Aerofoil," *New Scientist,* vol. 103, no. 1419, pp. 31-33, 30 August 1984.

[9] W. McKinney and J. DeLaurier, "Wingmill: An Oscillating-Wing Windmill," *Journal of energy,* vol. 5, no. 2, pp. 109-115, 1981.

[10] K. D. Jones, K. Lindsey and M. F. Platzer, "An Investigation of the Fluid-Structure Interaction in an Oscillating-Wing Micro-Hydropower Generator," in *Fluid Structure Interaction II,* Southampton, UK, WIT Press, 2003, pp. 73-82.

[11] D.-A. Wang, C.-Y. Chiu and H.-T. Pham, "Electromagnetic Energy Harvesting from Vibrations Induced by Kármán Vortex Street," *Mechatronics,* 2012.

[12] M. M. Bernitsas, K. Raghavan, Y. Ben-Simon and E. M. H. Garcia, "VIVACE Vortex Induced Vibration Aquatic Clean Energy: A New Concept in Generation of Clean and Renewable Energy From Fluid Flow," *Journal of Offshore Mechanics and Arctic Engineering*, vol. 130, no. 4, pp. 041101-15, 2008.

[13] S. M. Frayne, "Windbelt Innovation: Micro," Humdinger Wind Energy, 2008. [Online]. Available: http://www.humdingerwind.com/#/wi_micro/. [Accessed 11 January 2012].

[14] L. Tang, M. P. Paidoussis and J. Jiang, "Cantilevered Flexible Plates in Axial Flow: Energy Transfer and the Concept of Flutter-Mill," *Journal of Sound and Vibration*, vol. 326, p. 263–276, 2009.

[15] Q. Zhu, M. Haase and C. H. Wu, "Modeling the Capacity of a Novel Flow-Energy Harvester," *Applied Mathematical Modelling*, vol. 33, no. 5, pp. 2207-2217, May 2009.

[16] A. Barrero-Gil, G. Alonso and A. Sanz-Andres, "Energy Harvesting from Transverse Galloping," *Journal of Sound and Vibration*, vol. 329, no. 14, p. 2873–2883, July 2010.

[17] H.-J. Jung, S.-W. Lee and D.-D. Jang, "Feasibility Study on a New Energy Harvesting Electromagnetic Device Using Aerodynamic Instability," *IEEE Transactions on Magnetics*, vol. 45, no. 10, pp. 4376-4379, October 2009.

[18] A. Bibo, G. Li and M. F. Daqaq, "Electromechanical Modeling and Normal Form Analysis of an Aeroelastic Micro-Power Generator," *Journal of Intelligent Material Systems and Structures*, vol. 22, no. 6, pp. 577-592, April 2011.

[19] J. Sirohi and R. Mahadik, "Piezoelectric Wind Energy Harvester for Low-Power Sensors," *Journal of Intelligent Material Systems and Structures* , vol. 22, no. 18, pp. 2215-2228, December 2011.

[20] F. B. Farquharson, Aerodynamic Stability of Suspension Bridges: with Special Reference to the Tacoma Narrows Bridge, Washington: University of Washington, 1954.

[21] H.-J. Jung and S.-W. Lee, "The Experimental Validation of A New Energy Harvesting System Based on The Wake Galloping Phenomenon," *Smart Materials and Structures*, vol. 20, no. 5, 2011.

[22] E. H. Dowell, "Flutter of a Buckled Plate as an Example of Chaotic Motion of a Deterministic Autonomous System," *Journal of Sound and Vibration,* vol. 85, no. 3, pp. 333-344, 1982.

[23] J. P. Den Hartog, "Self Excited Vibrations," in *Mechanical Vibrations*, Courier Dover Publications, 1956, pp. 299-310.

[24] R. D. Blevins, Flow-Induced Vibration, 2nd Edition ed., New York: Van Nostrand Reinhold, 1990.

[25] T. R. Chandrupatla and A. D. Belegundu, Introduction to Finite Elements in Engineering, 3rd ed. ed., Upper Saddle River: Prentice Hall, 2002.

[26] C. De Marqui Junior, A. Erturk and D. J. Inman, "An Electromechanical Finite Element Model for Piezoelectric Energy Harvester Plates," *Journal of Sound and Vibration,* vol. 327, no. 1, pp. 9-25, October 2009.

[27] V. Mukhopadhyay and J. Dugunkji, *Wind Excited Vibration of Square Section Beam and Suspended Cable,* Massachusetts Institute of Technology, 1972.

[28] I. Robertson, L. Li, S. J. Sherwin and P. W. Bearman, "A Numerical Study of Rotational and Transverse Galloping Rectangular Bodies," *Journal of Fluids and Structures,* vol. 17, p. 681–699, 2003.

[29] H. Lindner, "Simulation of the Turbulence Influence on Galloping Vibrations," *Journal of Wind Engineering and Industrial Aerodynamics,* Vols. 41-44, pp. 2023-2034, 1992.

[30] G. Poulin, E. Sarraute and F. Costa, "Generation of Electrical Energy for Portable Devices Comparative Study of an Electromagnetic and a Piezoelectric System," *Sensors and Actuators,* vol. 116, no. 3, pp. 461-471, October 2004.

APPENDIX A: DERIVATION OF BEAM MASS AND STIFFNESS MATRICES

For a uniform beam element following Euler-Bernoulli theory, each node has translational and rotational displacements. Given below is the derivation for the mass and stiffness matrices for this beam element as explained by Chandrupatla [25].

The transverse displacement of any point within the element can be assumed to follow a cubic equation as follows.

$$w(x,t) = a_0(t) + a_1(t)x + a_2(t)x^2 + a_3(t)x^3 \tag{21}$$

$a_0(t)$, $a_1(t)$, $a_2(t)$ and $a_3(t)$ must satisfy the following conditions

$$\begin{aligned} w(0,t) &= \delta_1(t) \\ \dot{w}(0,t) &= \delta_2(t) \\ w(l_e,t) &= \delta_3(t) \\ \dot{w}(l_e,t) &= \delta_4(t) \end{aligned}$$

This will yield the following equations

$$\begin{aligned} a_0(t) &= \delta_1(t) \\ a_1(t) &= \delta_2(t) \\ a_2(t) &= \tfrac{1}{{l_e}^2}[-3\delta_1(t) - 2l_e\delta_2(t) + 3\delta_3(t) - l_e\delta_4(t)] \\ a_3(t) &= \tfrac{1}{{l_e}^3}[2\delta_1(t) + l_e\delta_2(t) - 2\delta_3(t) + l_e\delta_4(t)] \end{aligned} \tag{22}$$

By substituting Equation (22) into Equation (21)

$$w(x,t) = \left(1 - 3\frac{x^2}{l_e{}^2} + 2\frac{x^3}{l_e{}^3}\right)\delta_1(t) + \left(\frac{x}{l_e} - 2\frac{x^2}{l_e{}^2} + \frac{x^3}{l_e{}^3}\right)l_e\delta_2(t) + \left(3\frac{x^2}{l_e{}^2} - 2\frac{x^3}{l_e{}^3}\right)\delta_3(t) + \left(-\frac{x^2}{l_e{}^2} + \frac{x^3}{l_e{}^3}\right)l_e\delta_4(t) \quad (23)$$

This can be expressed as

$$w(x,t) = \lfloor N \rfloor \{\delta\} \quad (24)$$

Where

$$\lfloor N \rfloor = \left[\left(1 - 3\frac{x^2}{l_e{}^2} + 2\frac{x^3}{l_e{}^3}\right), \left(\frac{x}{l_e} - 2\frac{x^2}{l_e{}^2} + \frac{x^3}{l_e{}^3}\right)l_e, \left(3\frac{x^2}{l_e{}^2} - 2\frac{x^3}{l_e{}^3}\right), \left(-\frac{x^2}{l_e{}^2} + \frac{x^3}{l_e{}^3}\right)l_e\right] \quad (25)$$

The Kinetic Energy of the system can be expressed as:

$$K.E = \frac{1}{2}\int_0^{l_e} \rho A \left(\frac{\partial w(x,t)}{\partial t}\right)^2 dx = \frac{1}{2}\lfloor \dot{\delta}^T \rfloor [M_e]\{\dot{\delta}\} \quad (26)$$

Substituting Equation (24) into Equation (26) element mass matrix can be calculated as follows:

$$[M_e] = \rho A \int_0^{l_e} \{N^T\}\lfloor N \rfloor dx \quad (27)$$

Substituting Equation (25) into Equation (27) and integrating over the element length

$$[\mathrm{M_e}] = \frac{\rho \mathrm{A} l_e}{420}\begin{bmatrix} 156 & 22l_e & 54 & -13l_e \\ 22l_e & 4l_e{}^2 & 13l_e & -3l_e{}^2 \\ 54 & 13l_e & 156 & -22l_e \\ -13l_e & -3l_e{}^2 & -22l_e & 4l_e{}^2 \end{bmatrix}$$

The Strain Energy of the system can be expressed as:

$$S.E. = \frac{1}{2}\int_0^{l_e} EI \left(\frac{\partial^2 w(x,t)}{\partial x^2}\right)^2 dx = \frac{1}{2}\lfloor \dot{\delta}^T \rfloor [K_e]\{\dot{\delta}\} \quad (28)$$

Substituting Equation (24) into Equation (28) element stiffness matrix can be calculated as follows:

$$[K_e] = EI \int_0^{l_e} \left\{\frac{\partial^2 N}{\partial x^2}^T\right\} \left[\frac{\partial^2 N}{\partial x^2}\right] dx \qquad (29)$$

Substituting Equation (25) into Equation (29), getting the second partial derivative with respect to *x* then integrating over the element length we get the following equation

$$[\mathrm{K_e}] = \frac{\mathrm{EI}}{\mathrm{l_e}^3}\begin{bmatrix} 12 & 6\mathrm{l_e} & -12 & 6\mathrm{l_e} \\ 6\mathrm{l_e} & 4\mathrm{l_e}^2 & -6\mathrm{l_e} & 2\mathrm{l_e}^2 \\ -12 & -6\mathrm{l_e} & 12 & -6\mathrm{l_e} \\ 6\mathrm{l_e} & 2\mathrm{l_e}^2 & -6\mathrm{l_e} & 4\mathrm{l_e}^2 \end{bmatrix}$$

APPENDIX B: TIME DOMAIN VOLTAGE PLOTS FOR THE REMAINING MODEL VERIFIED EXPERIMENTAL RUNS

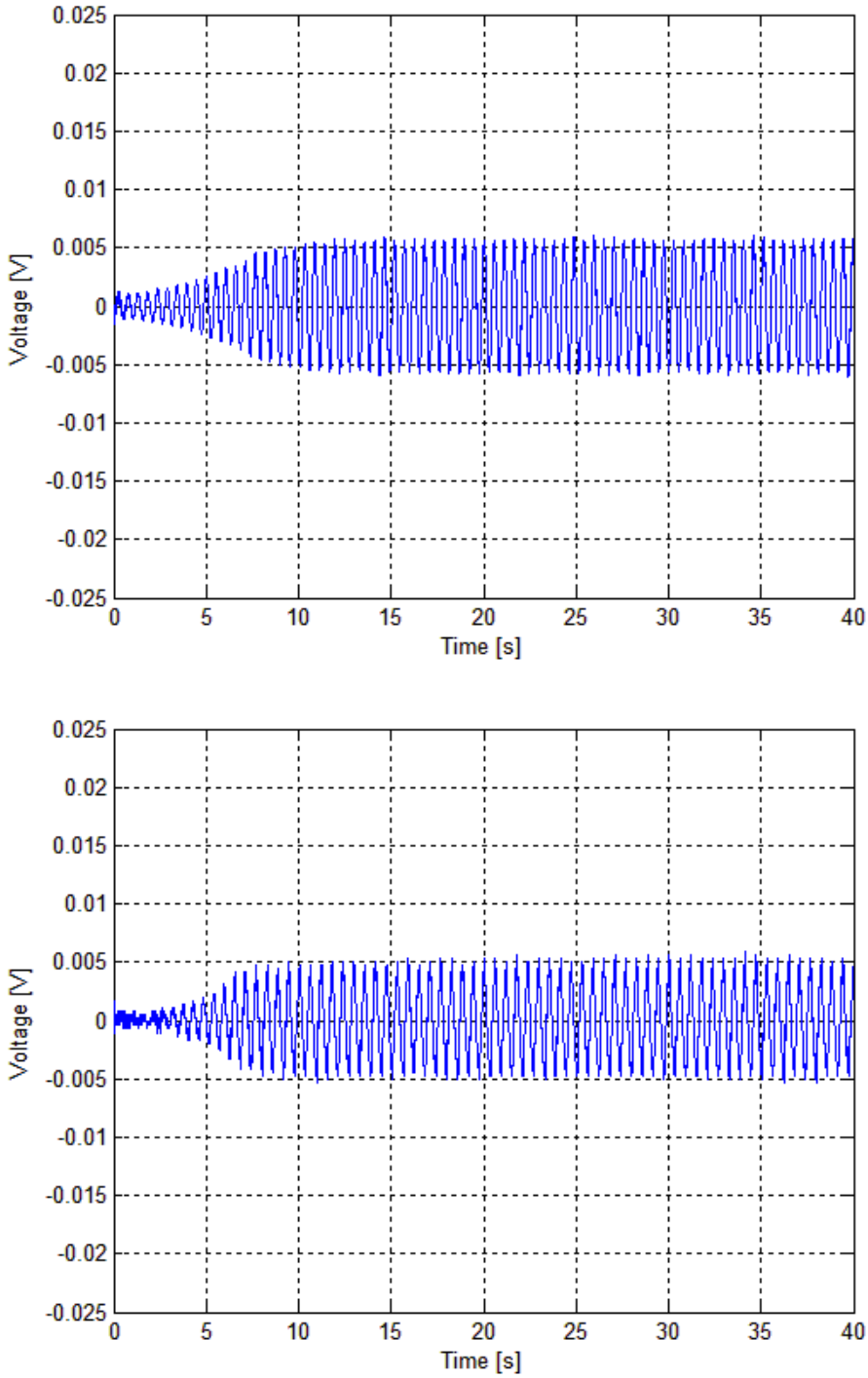

Figure 27: On top is the model predicted time response for the system using 40 ohm resistance at the wind speed of 2.3 m/s and below it is the experimentally measured response for it

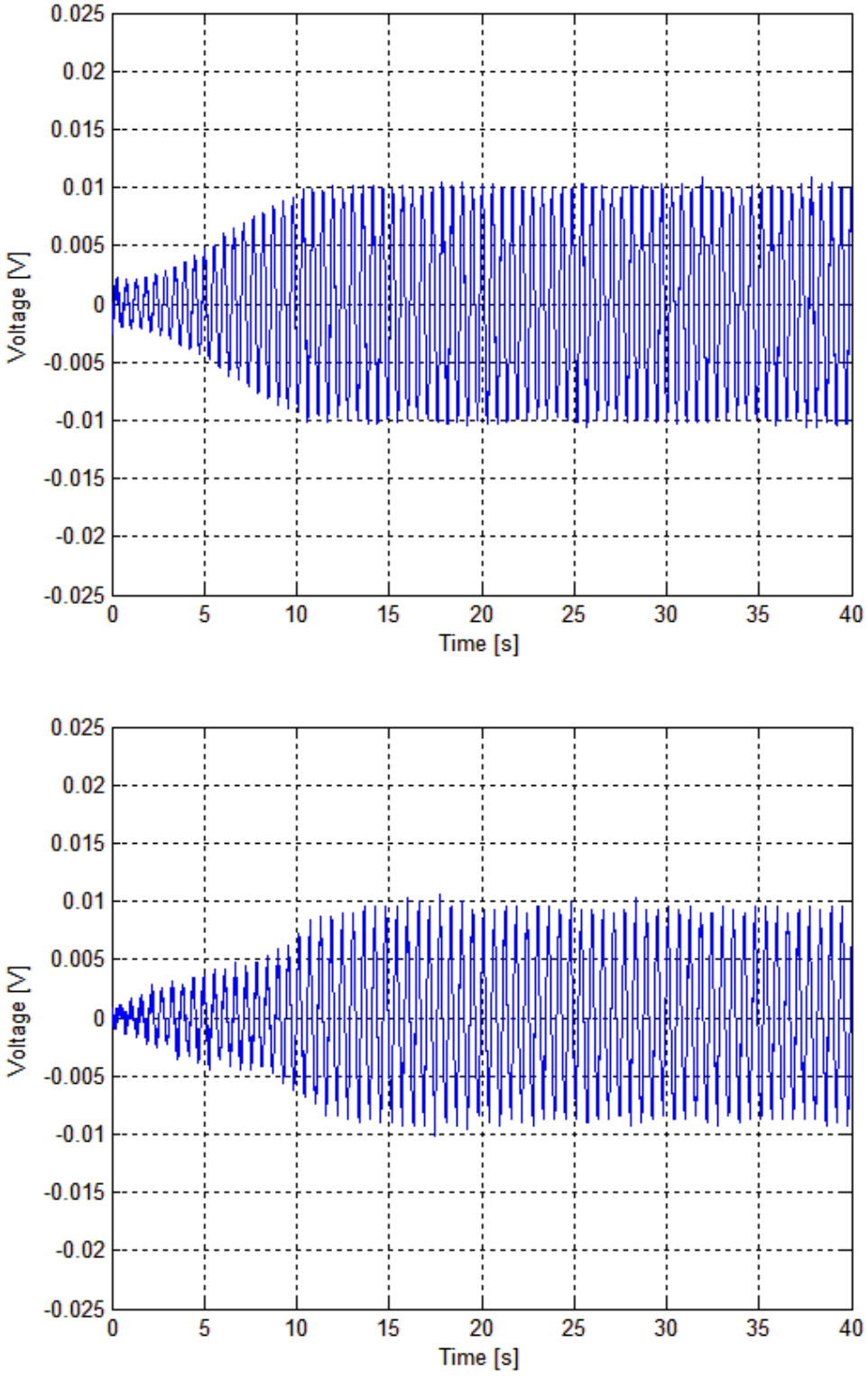

Figure 28: On top is the model predicted time response for the system using 100 ohm resistance at the wind speed of 2.3 m/s and below it is the experimentally measured response for it

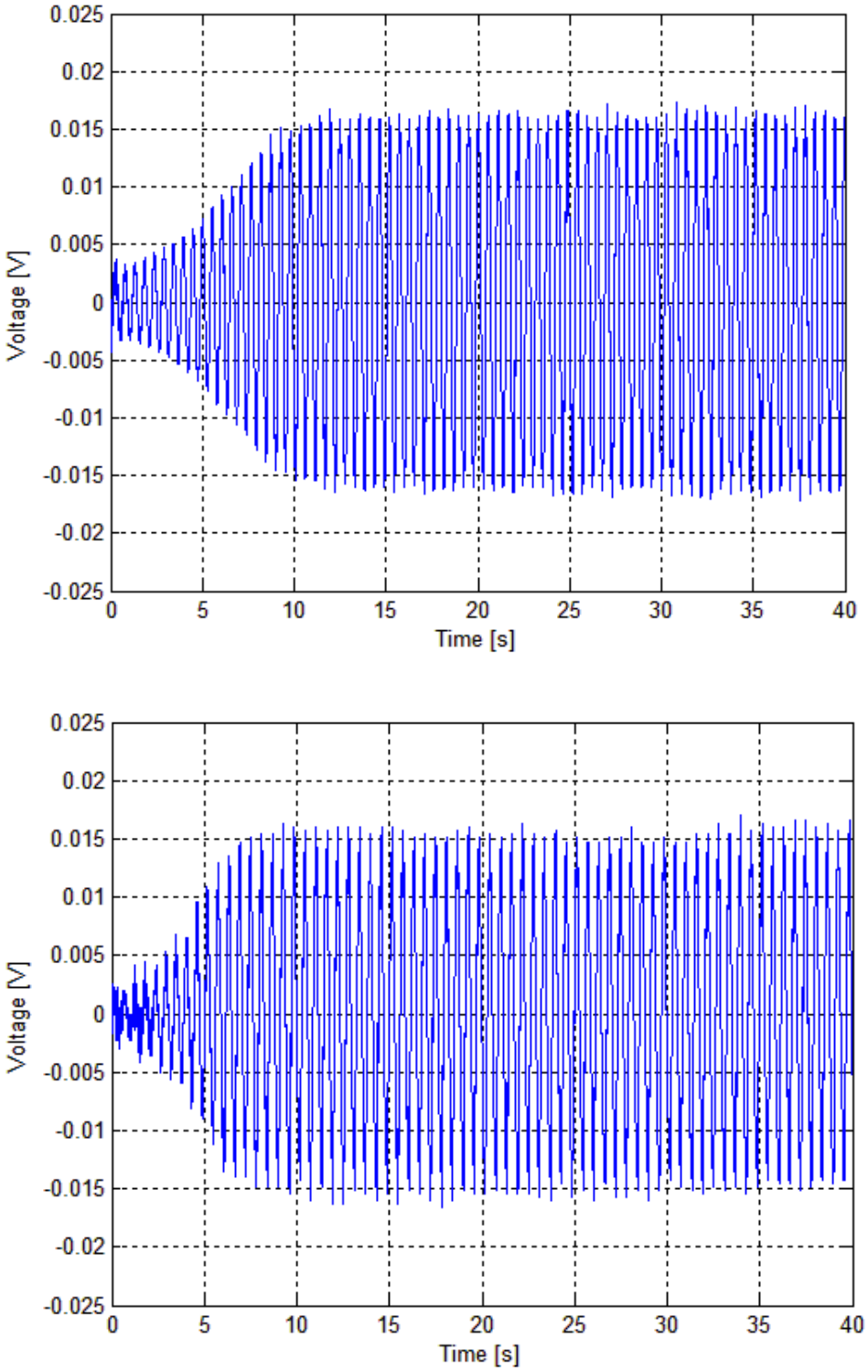

Figure 29: On top is the model predicted time response for the system using 400 ohm resistance at the wind speed of 2.3 m/s and below it is the experimentally measured response for it

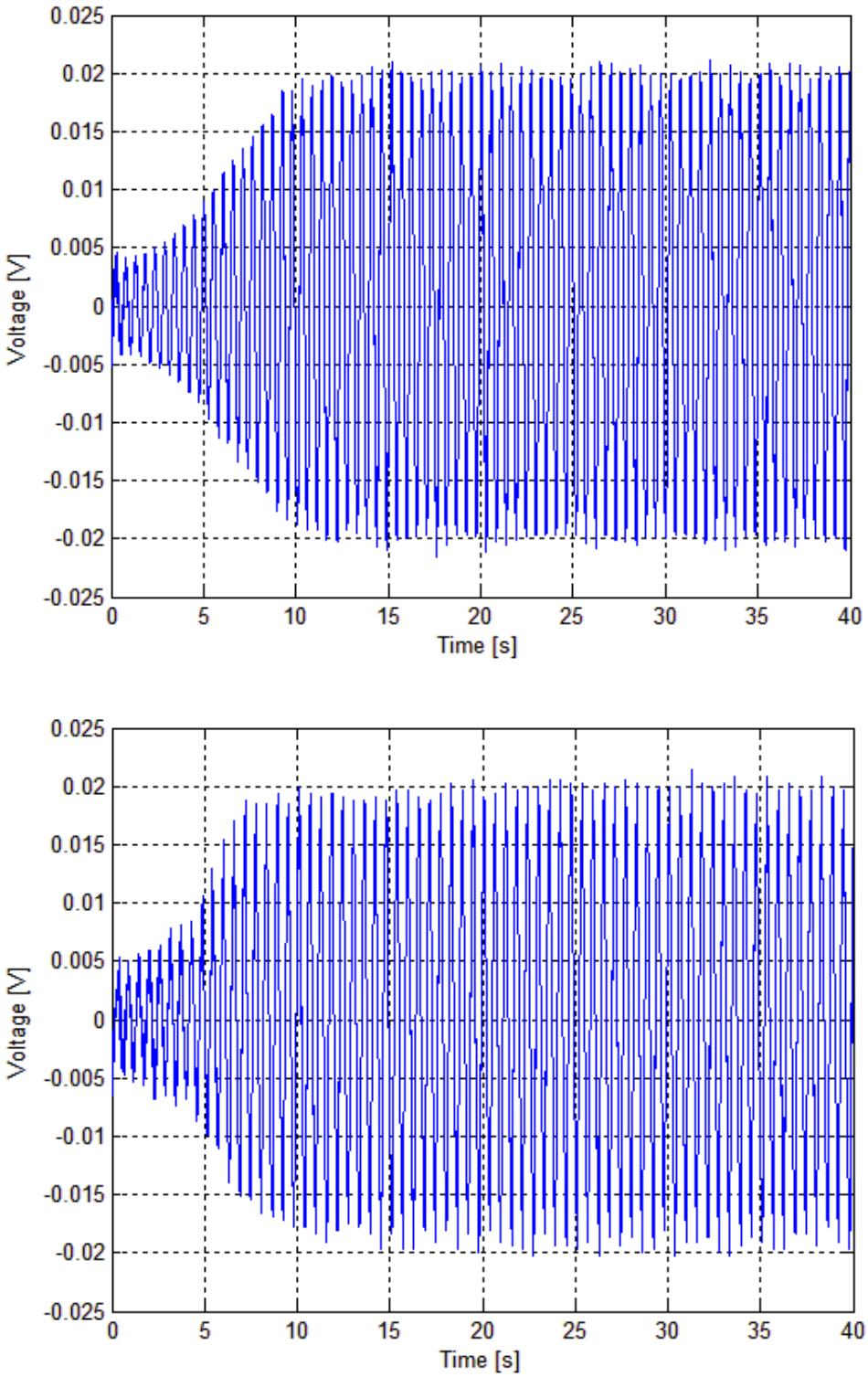

Figure 30: On top is the model predicted time response for the system using 4 Kohm resistance at the wind speed of 2.3 m/s and below it is the experimentally measured response for it

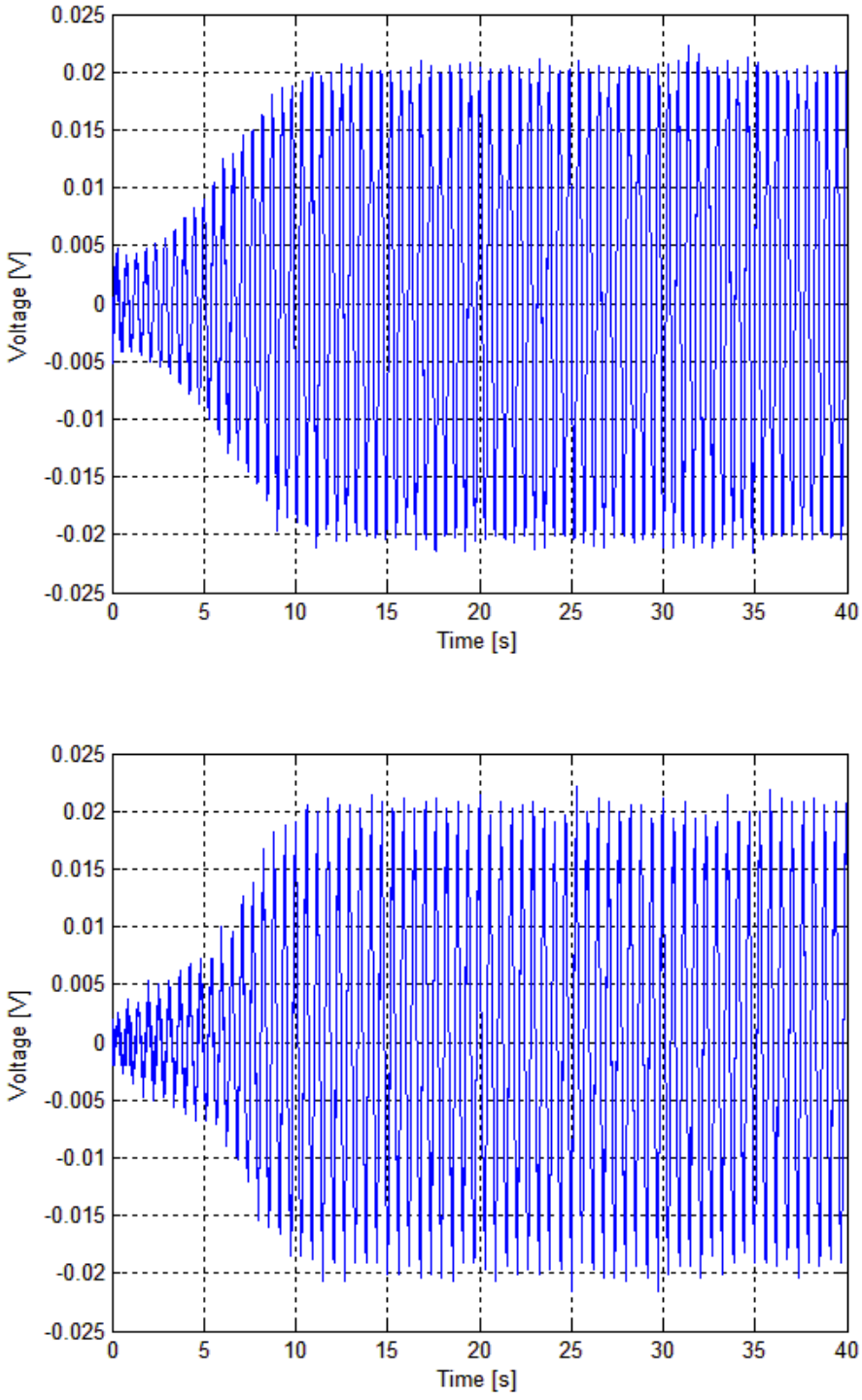

Figure 31: On top is the model predicted time response for the system using 4 Mohm resistance at the wind speed of 2.3 m/s and below it is the experimentally measured response for it

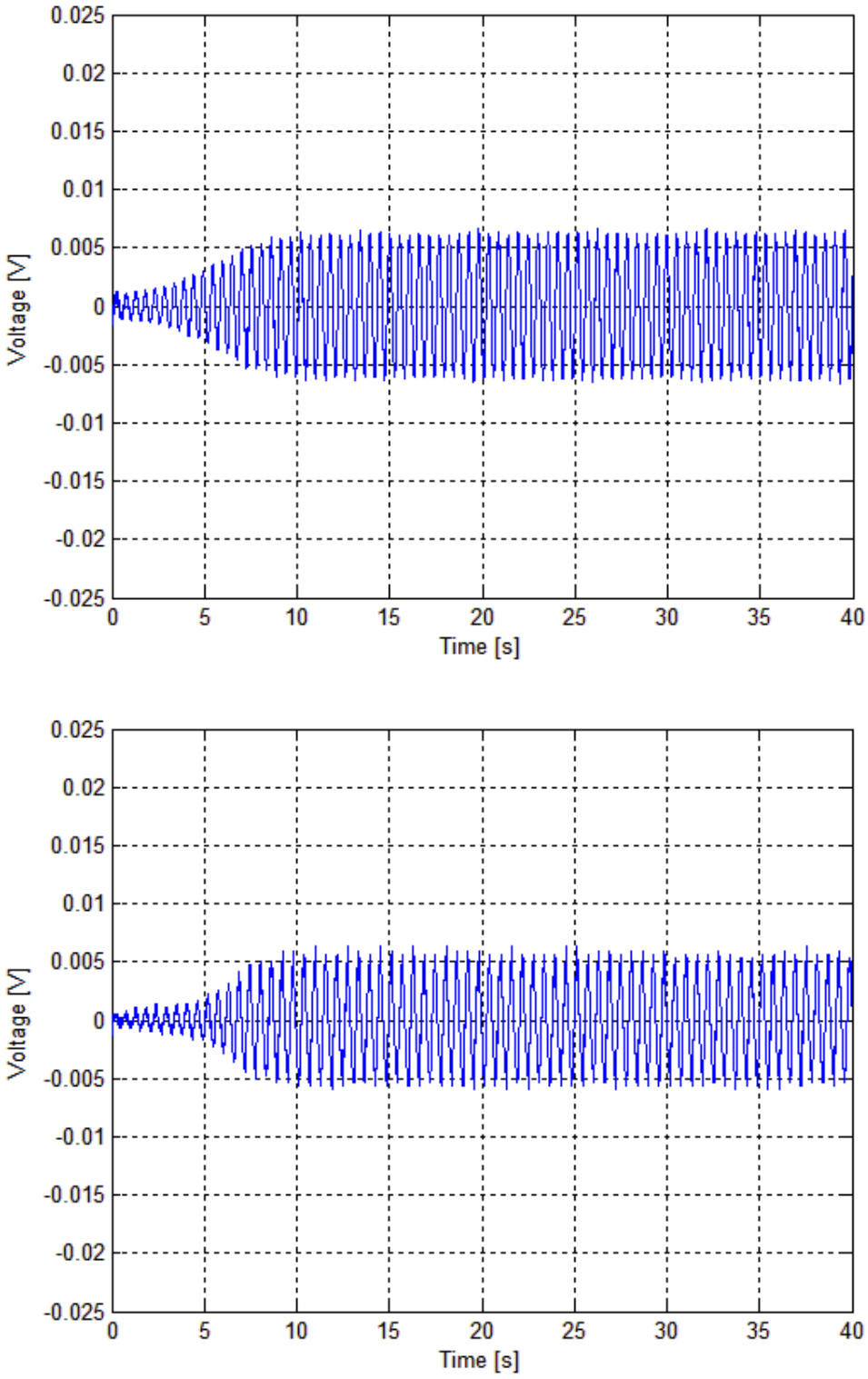

Figure 32: On top is the model predicted time response for the system using 40 ohm resistance at the wind speed of 2.7 m/s and below it is the experimentally measured response for it

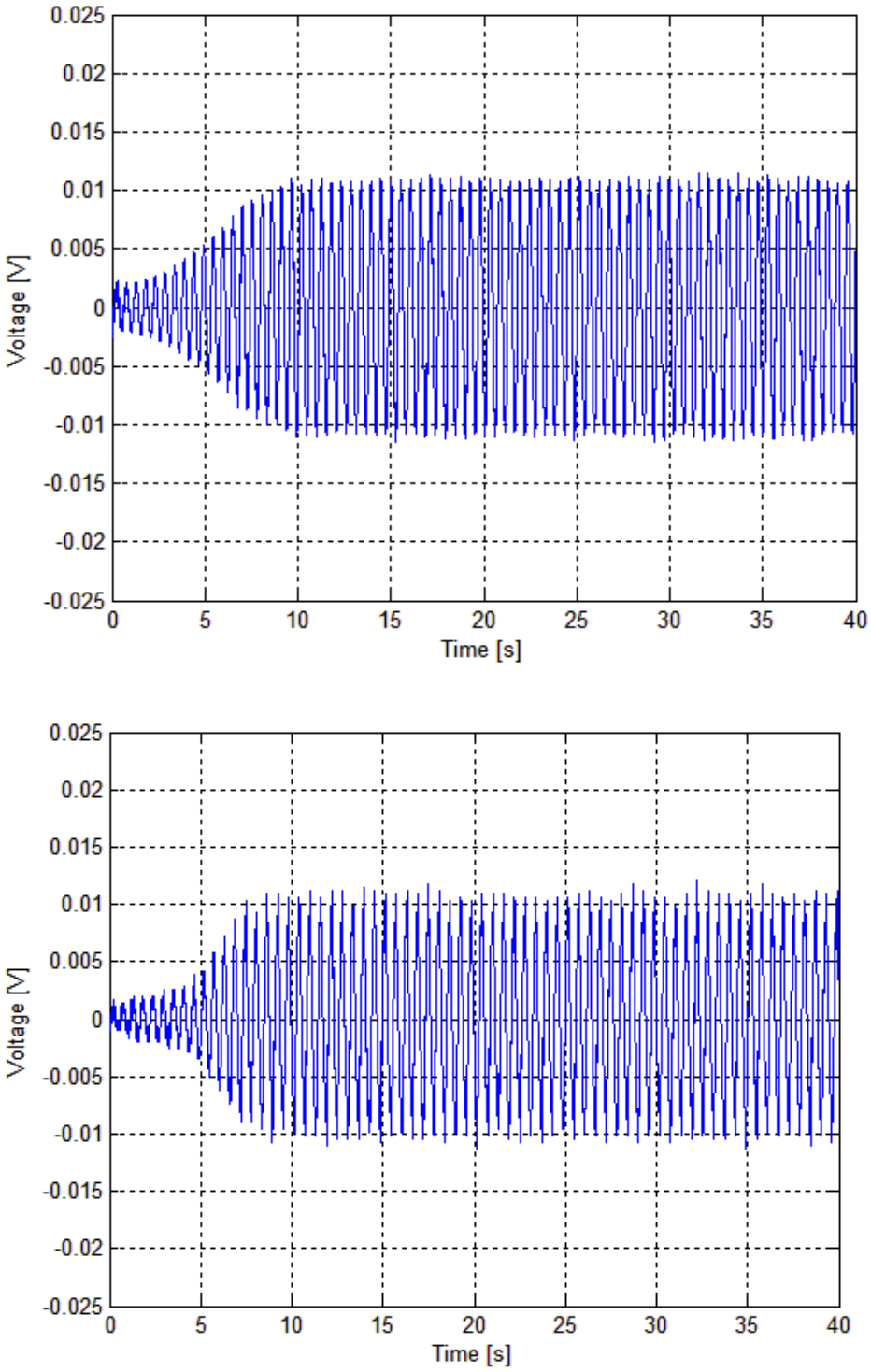

Figure 33: On top is the model predicted time response for the system using 100 ohm resistance at the wind speed of 2.7 m/s and below it is the experimentally measured response for it

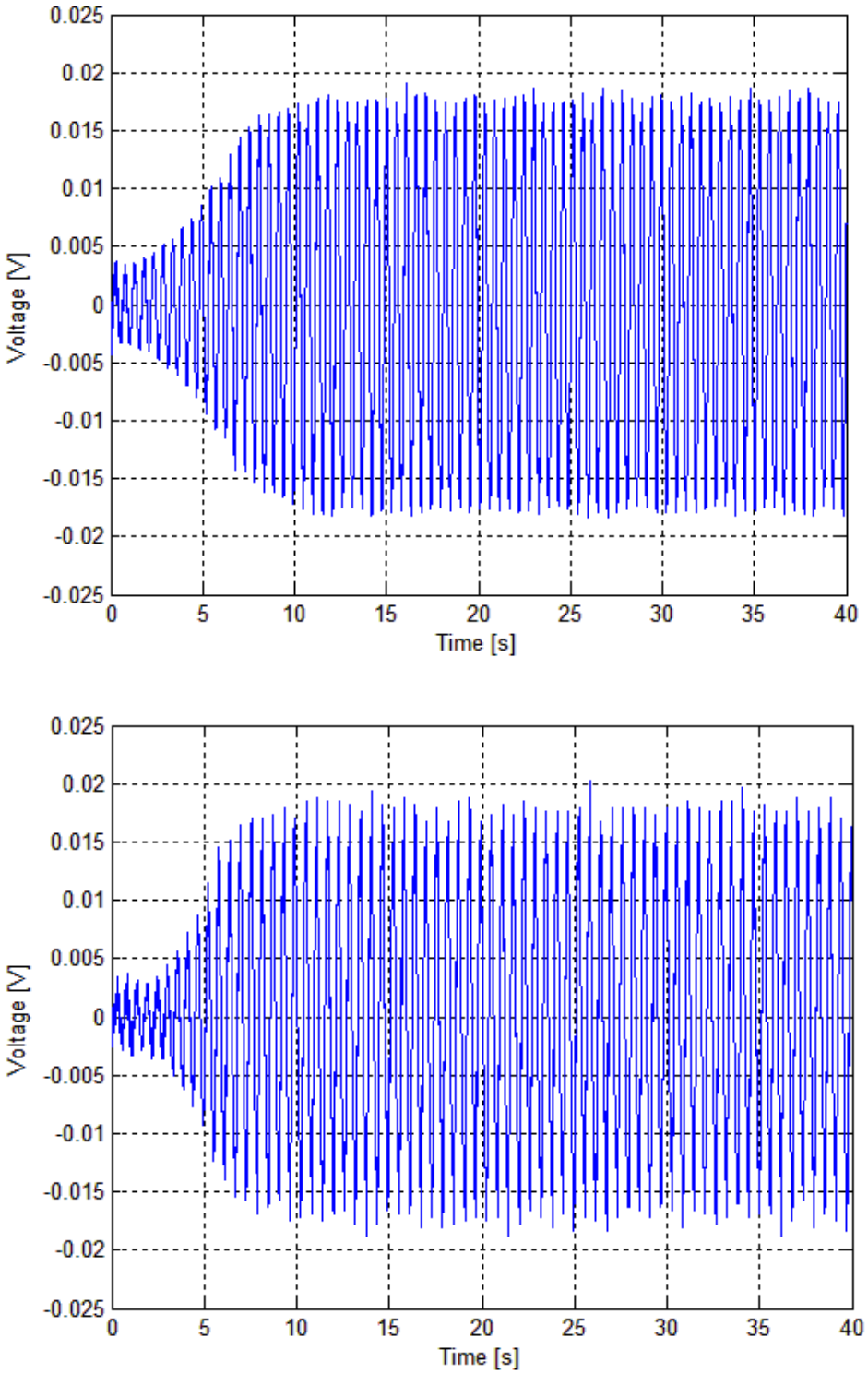

Figure 34: On top is the model predicted time response for the system using 400 ohm resistance at the wind speed of 2.7 m/s and below it is the experimentally measured response for it

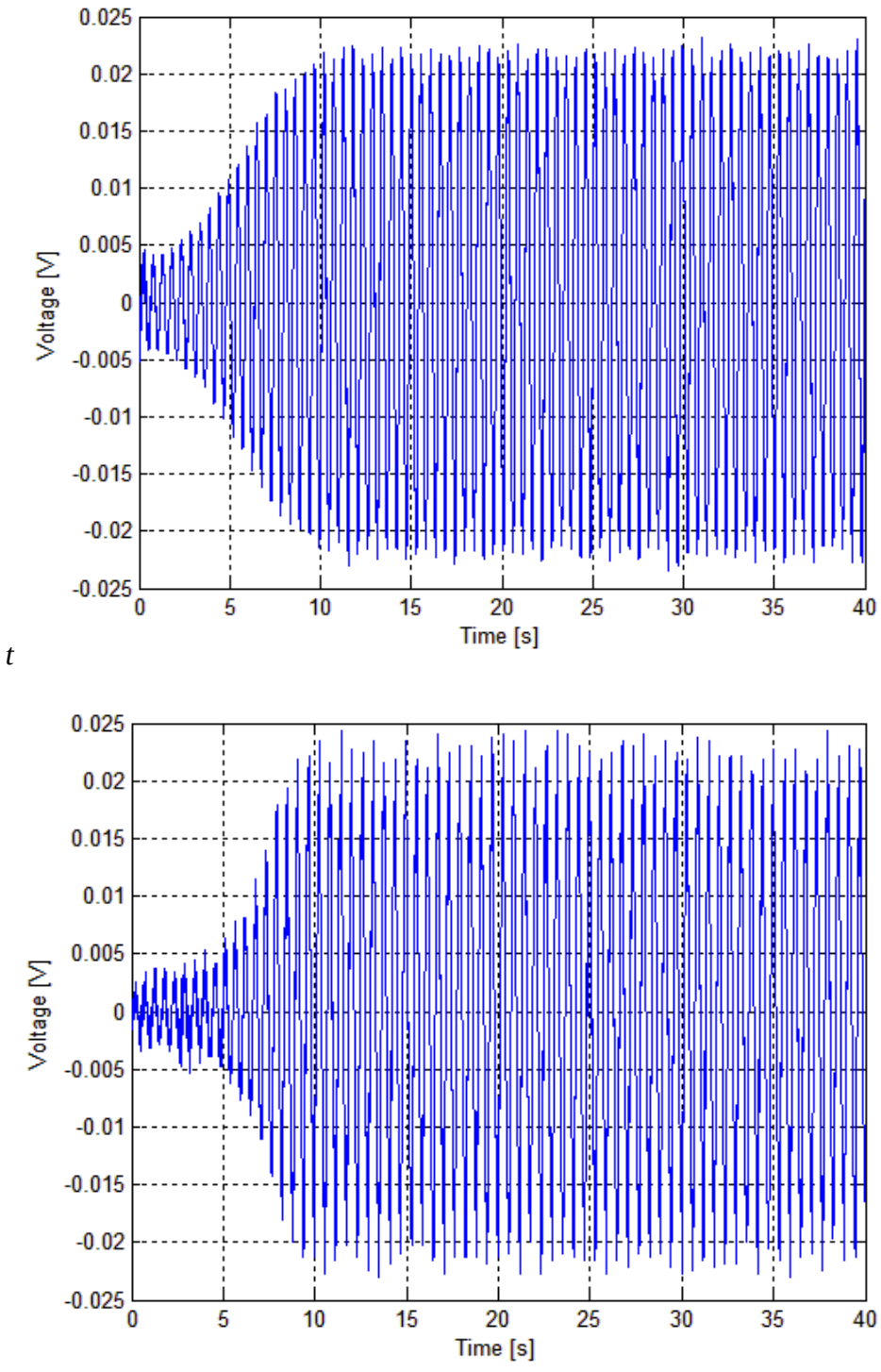

t

Figure 35: On top is the model predicted time response for the system using 4 Kohm resistance at the wind speed of 2.7 m/s and below it is the experimentally measured response for it

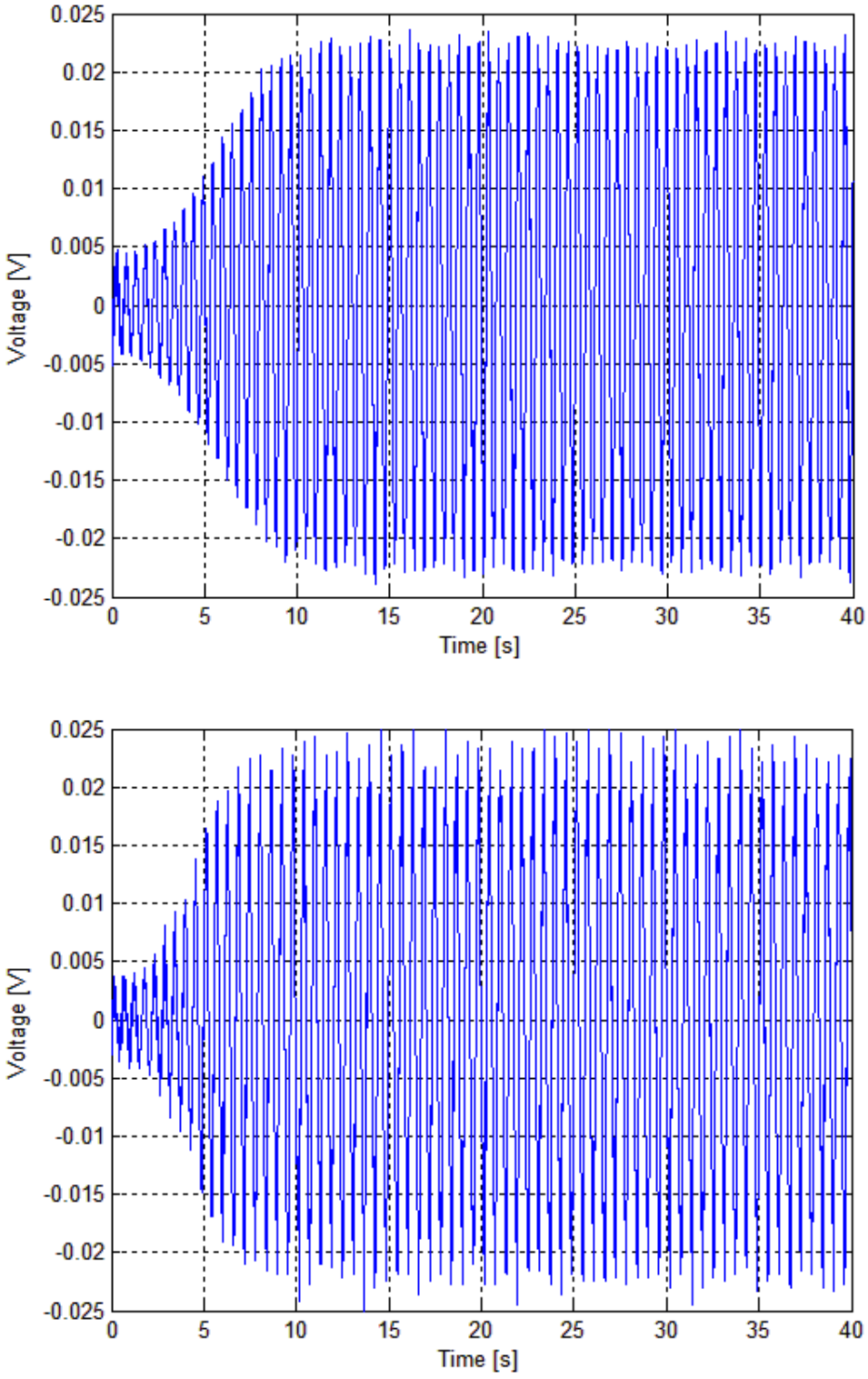

Figure 36: On top is the model predicted time response for the system using 4 Mohm resistance at the wind speed of 2.7 m/s and below it is the experimentally measured response for it

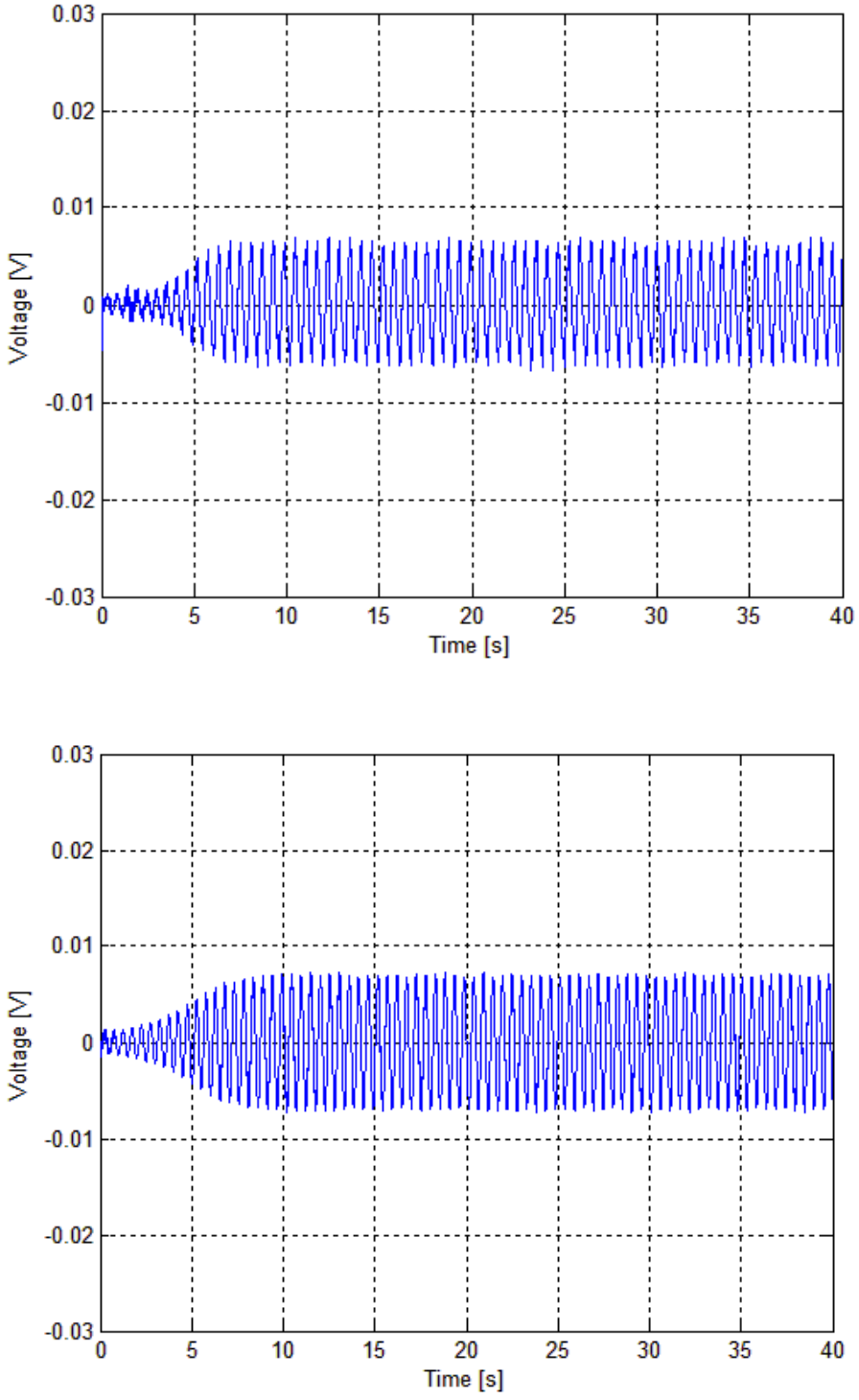

Figure 37: On top is the model predicted time response for the system using 40 ohm resistance at the wind speed of 3.2 m/s and below it is the experimentally measured response for it

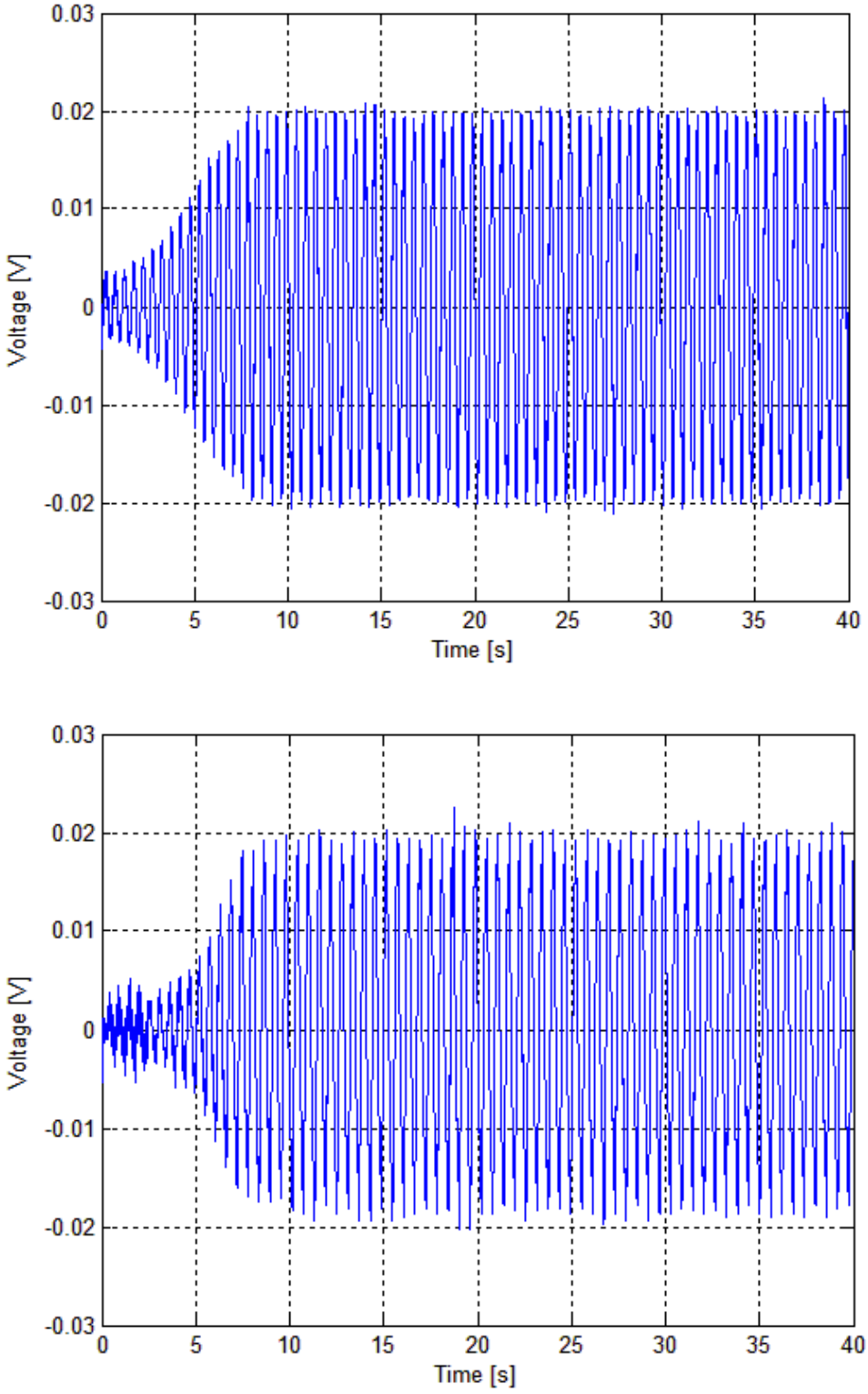

Figure 38: On top is the model predicted time response for the system using 400 ohm resistance at the wind speed of 3.2 m/s and below it is the experimentally measured response for it

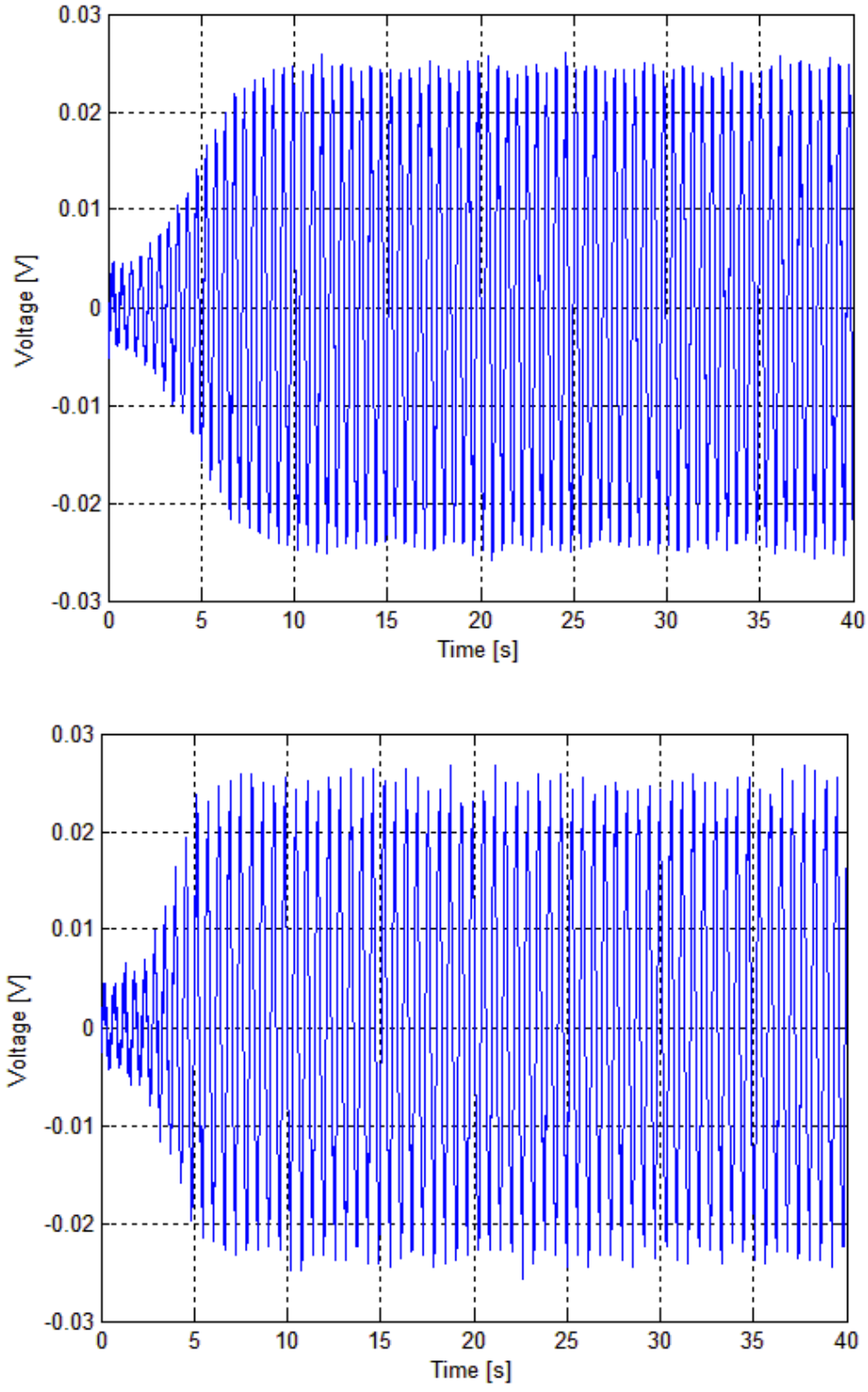

Figure 39: On top is the model predicted time response for the system using 4 Kohm resistance at the wind speed of 3.2 m/s and below it is the experimentally measured response for it

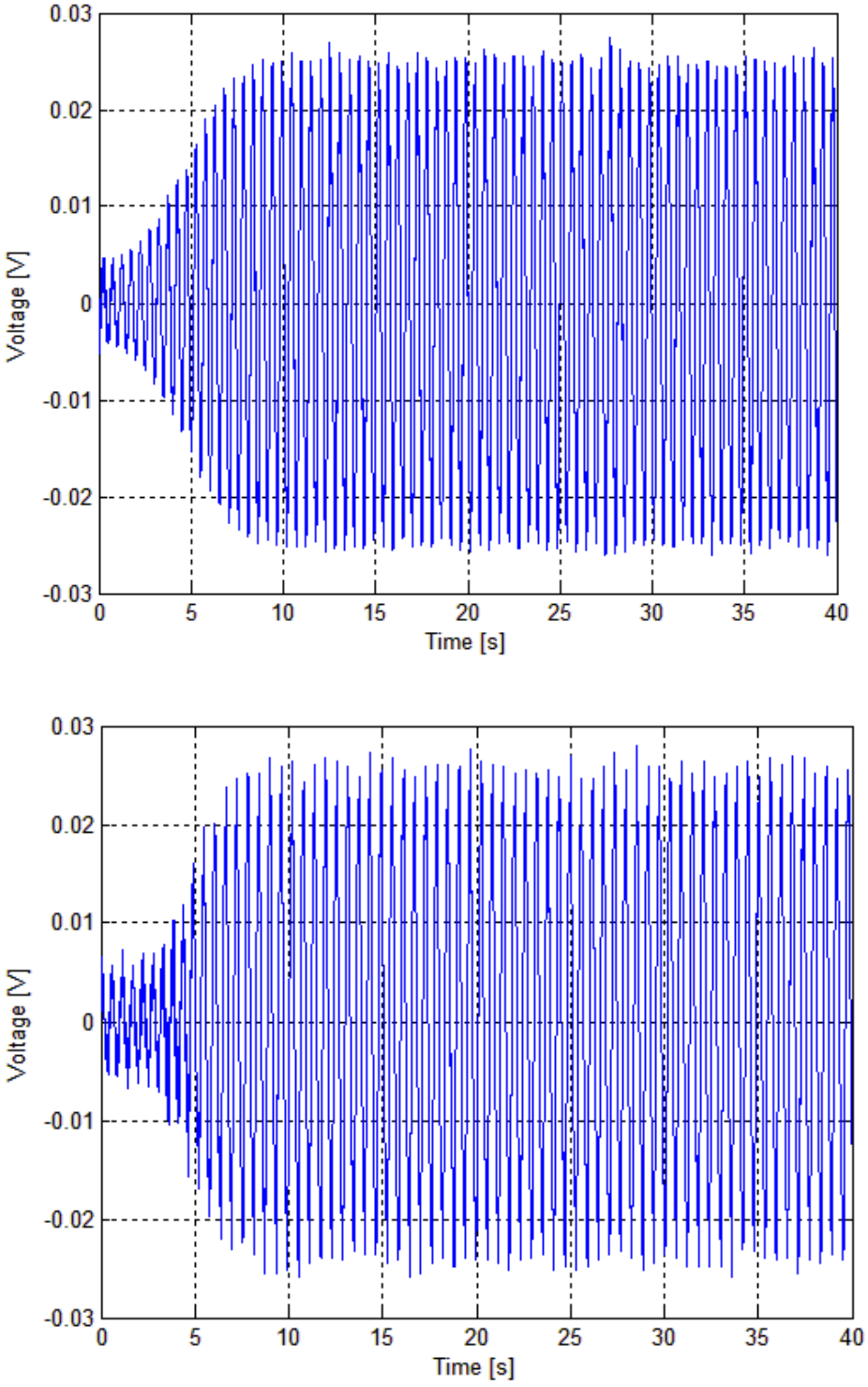

Figure 40: On top is the model predicted time response for the system using 4 Mohm resistance at the wind speed of 3.2 m/s and below it is the experimentally measured response for it